Mikhail Lyubomirskiy

High energy X-ray inline interferometry based on refractive optics

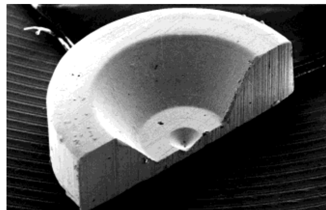

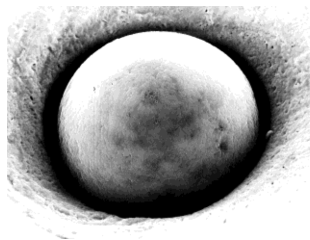

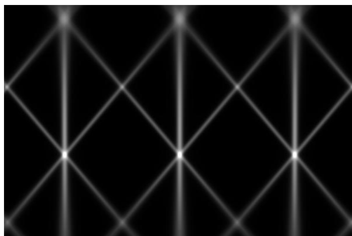

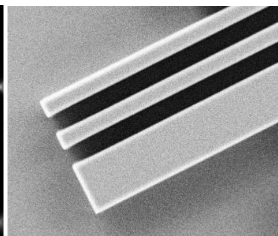

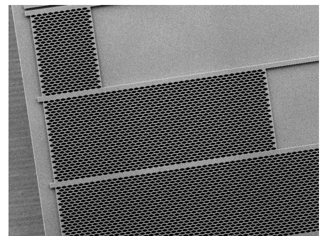

Acknowledgments

I would like to express my thanks to people who have helped me made this thesis. First of all I want deeply thank my thesis supervisor – Dr. Anatoly Snigirev, who initiated the project I worked on. For his willingness for scientific discussion, support of new ideas and for many interesting lectures about X-ray optics, almost all I know about X-ray refractive optics I know because of him. Anatoly motivates everyone in the group just by sharing new ideas and plans (not necessarily about science) that comes up every day. His contribution to my work cannot be overestimated.

I warmly thank his wife - Irina Snigireva for constant help during my time at the ESRF, she always has been ready to provide tiny equipment that I needed for the experiment. Irina always was ready “to check” details with SEM even at 11 pm of Sunday during beamtime. Irina is the best companion for writing scientific articles; she never missed any mistakes or illogic in my texts.

Many thanks to Viktor Kohn for simulations of lens based interferometers, and for many interesting discussions about coherent optics and wave propagation.

I would like to acknowledge Carsten Detlefs for his constant support at the beamline ID06 and for his comments on this thesis.

I am thankful to my collaborators from Chernogolovka: Sergey Kuznetsov for discussions about surface roughnesses models and Vyacheslav Yunkin for providing high quality etched Si structures.

I want to thank Ken Vidar Falch for his readiness for different scientific discussions and sharing an opinion about my work.

My gratitude goes to Pierre Wattecamps for engineering support at ID06 beamline; he was always ready to build something for my experiments.

I am grateful to Agnieszka Witkowska for accepting to be my thesis promoter and for proofreading of my thesis.

I thank Dmitry Belov and Petr Ershov for spending many unforgettable night shifts with me at the beamline.

My special thanks goes to Damian Paliwoda for assistance with proofreading.

Finally I want to express my gratitude to Gavin Vaughan who helped me to perform high energy experiments at ID11 beamline.

Abstract

The dissertation is directed toward advancing the field of hard X-ray interferometry by contributing the development and characterization of interferometers. It is mainly concentrated on interferometers based on reflection and refraction of X-rays that are fabricated by MEMS technology in Si crystals. The development, characterization and application of three new interferometric schemes in the hard X-ray region are performed.

Understanding the spatial coherence properties of X-ray radiation is increasingly required for the design and manufacturing of x-ray optical elements, and for planning and analyzing experiments. Therefore, as one part of this work a new interferometric scheme based on the Young double slit technique was implemented in order to accurately characterize the transverse coherence at the beamline ID06 at the ESRF. The result of these measurements is expanded an understanding of sensitivity of interferometric techniques to the photon source size fluctuations at the low emittance storage rings. This technique allows measuring the source size with a very compact set-up.

The next scheme explored in this thesis is a multi-lens interferometer. Two interferometers, consisting of 30 and 6 lens arrays, were manufactured in Si crystals and experimentally tested. The tests have been performed over a wide energy range – from 12 to 64 keV.

Experimental results showed full agreement with theory which confirms that the quality of manufacturing is good enough to not contaminate interference patterns formed by interferometers based on refraction of X-rays.

The effective source size was determined with high precision by analyzing the fundamental Talbot image formed by the multi-lens interferometer using high photon energies. The particularity that an interference pattern is formed in the far field allows one to use this interferometer as a tool to diagnose the sphericity of the incident wavefront. In addition such lens array could be used as an advanced Shack-Hartmann wavefront sensor in focusing mode.

The possibility of forming a standing wave in paraxial geometry with variable period and maxima width opened up the new perspective of using this interferometer for the purpose of the investigation of nano objects without deposition on a flat surface (in contrast to the reflectivity or

diffraction based standing wave technique). The large depth of field of interference fringe (in comparison to the focal spot of the same size) expands experimental possibilities in using this interferometer for the transmission scanning microscopy and Moiré radiography of nanoscale objects.

Moreover, there is a group of potential applications related to the beam conditioning. This interferometer can be used as a beam expander or versatile illuminator to provide coherent illumination of large scale object on free electron laser X-ray sources (FELs) or ultimate storage rings.

Finally the lens array based interferometers may be used for phase contrast imaging.

Last, but not least, an interferometric scheme is a single crystal double mirror. It was discovered, during the study of the optical properties of multilens interferometers, that quality of the etched surface of structures is high enough to obtain total external reflection of X-rays. Therefore a bi – mirror interferometer consisting of two parallel channels was manufactured on the same Si chip as six-lens interferometer.

The sensitivity of the interference contrast to the angle of incidence was discovered and used to evaluate the surface roughness. As the two reflective surfaces are located in close proximity high contrast interference pattern can be observed with sources with poor spatial coherence. This opened up prospects of using such interferometers under the conditions of lab sources.

Streszczenie w języku polskim

Rozprawa doktorska dotyczy rozwoju zaawansowanych technik interferometrii z użyciem wysokoenergetycznego promieniowania rentgenowskiego, a jej celem jest budowa i charakteryzacja interferometrów nowej generacji. Rozprawę poświęcono interferometrom działającym na zasadzie odbicia i refrakcji promieniowania rentgenowskiego oraz wykonanym w kryształach krzemu przy użyciu technologii MEMS. W ramach pracy skonstruowano, przetestowano i scharakteryzowano trzy nowe interferometry stosowane do badań w zakresie wysokoenergetycznego promieniowania rentgenowskiego. Możliwość kontroli spójności przestrzennej promieni X ma podstawowe znaczenie w projektowaniu i budowie elementów optycznych, a także w planowaniu eksperymentu i analizie danych. Celem rozprawy była konstrukcja nowych interferometrów Younga z podwójną szczeliną do precyzyjnego (w skali mikronowej) określenia rozmiaru wiązki fotonów na linii ID06 w ESRF w Grenoble. Wyniki wykonanych pomiarów pozwalają lepiej zrozumieć czułość technik interferometrycznych na fluktuacje źródła fotonów w pierścieniu akumulacyjnym o niskiej emitancji.

W ramach pracy doktorskiej zaprojektowano również interferometry wielosoczewkowe. Dwa z nich zbudowane zostały na bazie kryształów krzemu, odpowiednio z 30 i 6 soczewek, oraz przetestowane w zakresie energii – od 12 do 64 keV. Wyniki eksperymentalne w pełni zgadzają się z modelem teoretycznym, co świadczy o odpowiedniej jakości skonstruowanych interferometrów, które nie zaburzają interferencji uzyskanej w wyniku refrakcji promieniowania rentgenowskiego. Rozmiar efektywnego źródła fotonów został wyznaczony z wysoką precyzją poprzez zastosowanie fundamentalnej analizy Talbota z użyciem interferometrów wielosoczewkowych i fotonów wysokiej energii. Szczególnym osiągnieciem opisanym w rozprawie jest możliwość wykorzystania opisanych interferometrów w celach diagnostycznych do badania sferyczności fali

padającej. Dodatkowo, soczewki takie mogą być wykorzystane jako zaawansowane czujniki typu Shack-Hartmann.

Co wiecej, możliwość tworzenia równołeglej fali stojącej o zmiennym okresie i szerokości maksimum daje nowe perspektywy badawcze nanoobiektów bez konieczności ich osadzania na powierzchniach płaskich (w odróżnieniu od techniki wykorzystującej fale stojące utworzone w wyniku dyfrakcji lub odbicia). Wysoka głębia ostrości skonstruowanych interferometrów poszerza zakres ich możliwości eksperymentalnych w zakresie zastosowania w badaniach nanoobiektów metodami Transmisyjnej Mikroskopii Skaningowej oraz radiografii Moiré. Interferometry takie moga być również wykorzystane przy kondycjonowaniu wiązki promieniowania rentgenowskiego jako uniwersalne iluminatory obiektów o dużych rozmiarach w źródłach XFEL lub pierścieniach akumulacyjnych.

Interferometry wielosoczewkowe mogą mieć zastosowanie w technice obrazowania kontrastu fazowego. Interesującym przykładem jest tutaj interferometr monokrystaliczny z podwójnym zwierciadłem. W ramach niniejszej pracy eksperymentalnie dowiedziono wysoką jakość interferometrów wielosoczewkowych, które zdolne są do całkowitego odbicia promieni rentgenowskich. Na bazie tego samego monokrysztalu krzemu zbudowano dwa interferometry z podwójnym lustrem: z dwoma równoległymi kanałami oraz szescio-soczewkowy. Określono zależność czułości kontrastu interferencyjnego od kąta padania promieniowania, która może być użyta jako wyznacznik chropowatości powierzchni.

Opisane w ramach niniejszej pracy technologie i otrzymane wyniki otwierają nowe perspektywy użycia interferometrów w warunkach laboratoryjnych.

Contents

INTRODUCTION ... 10
1. Interaction of X-rays and a matter ... 12
1.1 Complex refractive index ... 12
1.2 Refraction and reflection of X-rays ... 15
1.3 Scattering of X-rays ... 16
2. Instrumentation ... 17
2.1 X-ray sources ... 17
2.1.1 X-ray tube ... 17
2.1.2 Synchrotron ... 19
2.1.2.1 Insertion devices ... 21
2.1.2.2 Emittance and source size ... 23
2.1.2.3 A beamline layout ... 23
2.2 The refractive lenses for X-rays ... 25
2.2.1 Focal length ... 26
2.2.2 Transmission and effective aperture of the lens ... 26
2.2.3 Depth of field and depth of focus ... 28
2.3. Si planar structures manufacturing ... 29
2.3.1 Electron beam lithography ... 29
2.3.2 Deep dry etching ... 30
3. Diffraction ... 33
3.1 The Fresnel-Kirchhoff diffraction formula ... 33
3.2 Fresnel diffraction ... 35
3.3 Fraunhofer diffraction ... 37
3.4 Diffraction on periodical objects – Talbot effect ... 39
4. Interference with partially coherent light ... 41
4.1 Coherence ... 41
4.1.2 Mutual coherence function ... 41
4.1.3 Temporal coherence ... 42
4.1.4 Transversal coherence ... 43
4.2 X-ray interferometry ... 45

4.2.1 Bonse – Hart interferometer 45
4.2.2 Double slit interferometer 46
4.2.3 Double mirror interferometer 47
4.2.4 Bilens interferometer 48
4.3 The study of coherence of synchrotron beam 50
5. The tunable double pinhole interferometer 53
5.1 Sensitivity to the source size fluctuation 53
5.2 The concept of the interferometer 56
5.3 Experiment 58
5.4 Discussion 63
6. Multilens interferometers 64
6.1 The concept of multilens interferometer 64
6.2 Theory 68
6.3 Multilens interferometers optical properties study 72
6.3.1 Sixlens interferometer 72
6.3.2 Thirty lens interferometer 77
6.4 Computer simulations 81
6.5 Discussion 84
6.6 Applications 85
7. Micro mirrors interferometer 86
7.1 The concept of the interferometer 87
7.2 The interferometer optical properties study 90
7.3 Applications 94
7.4 Discussion 98
8. Conclusions 99
List of symbols 101
List of abbreviations 104
Bibliography 105

INTRODUCTION

Coherence of two waves is the ability of these waves of showing constructive interference. The well known “phase problem” (it is only possible to record an amplitude of the wave, but not the phase) does not allows proper reconstruction of the object by illumination of it, recording and then analyzing the transmitted signal. The use of coherent beam is only one existing way to determine (or reconstruct) the phase shift caused by the object that wave has transmitted through.

Coherent radiation offers indispensable opportunities for science, technology and medicine. It, for example, provided diffraction-limited focusing (for scanning laser confocal microscopy) [1], enable convenient recording of interference patterns (interferometry) [2]. The coherent radiation has been readily available and widely utilized at visible light for many years [3-8], and it becomes available just couple of decades ago at hard X-rays region [9-17]. Because of transverse coherence is inversely proportional to the energy of irradiation, the requirements imposed to the X-ray sources are stricter.

The advent of dedicated storage rings – synchrotrons of 3rd generation provided coherent tunable hard X-ray beams with flux of several orders of magnitude higher than conventional X-ray sources. Wide availability of these highly coherent beams has triggered the rapid development of new type of optics for hard X-rays. The most famous examples are refractive lenses (RL) [18], and Fresnel zone plates (FZP) [19] for hard X-rays. Despite the fact that W.C. Röntgen concluded on the base of his experiments that X-rays could not be focused by refractive lenses, the first refractive lenses have been made in 1996 [18].

Coherent experimental techniques widely utilized in visible light just became possible to apply for hard X-rays. One of these techniques, for example, phase contrast imaging [10, 20] requires high spatial coherence of incoming X-ray beam. Moreover “classical” interferometric experiments such as Young double slit technique [21] or Talbot grating interferometry [22] were performed in X-ray region for the first time.

The development of X-ray coherent techniques is caused not only by the advent of modern sources but also by the wide availability of new high quality fabrication techniques and materials which were developed in the last couple of decades. Since the very beginning X-ray science played the key role in the success of development of material science and notably Si manufacturing and structuring technologies - it is the well known fact that five Nobel prizes were given for applications of X-rays in the direction of material research.

Now the situation is completely opposite, the success in material research and particularly in silicon industry is impacting the development of X-ray science. Perfect crystals of silicon are used for manufacturing of monochromators and mirrors for modern X-ray sources such as 3rd generation synchrotrons and FELs.

The modern technologies of micro electro mechanical systems (MEMS) allow to structure the Si crystal with high quality of the structured surfaces. The advent of the BOSCH etching process allowed manufacturing of deep Si structures with vertical sidewalls. This has resulted in possibility of manufacturing of nanofocusing lenses (NFLs) for hard X-rays and achieving a very small size of the focal spot [23]. This ability of creating very small focal spot – secondary source was implemented in designing of bilens interferometer [24] which consists of 2 parallel lens arrays and under coherent illumination forms standing wave with variable period.

This dissertation is directed toward advancing the field of hard X-ray interferometry by contributing the development and characterizing of interferometers on the base of Si planar technologies and its applications.

First 4 chapters are an introductory part. Chapter number 5 describes a new interferometric scheme based on Young technique that we developed in order to accurately characterize transverse coherence at the ID06 beamline at the ESRF. In addition our understanding of sensitivity of interferometric techniques to the source size fluctuations has been expanded.

Chapter 6 addresses multilens interferometers. It starts with the concept of interferometer and theory that explaining a process of forming of interference patterns. Then the experimental tests of optical properties are presented.

In chapter 7, concept and experimental tests of mirror based interferometers are presented. An experiment showed that there is an influence of mirror's surface roughness influence to the interference pattern. Therefore interferometer was used to estimate surface roughness.

Experimental results, analysis and future prospects are discussed in chapter 8.

1. Interaction of X-rays and a matter

X-rays have been discovered by Wilhelm Röntgen in 1895 [25]. A first application was absorption contrast imaging (radiography); Röntgen used the high penetration power of X-rays to observe the bones of the human body because the absorption is strongly dependent on the electron density of the material. Only a few years later X-rays would find widespread use in medicine.

Another important application is based on the diffraction phenomena showing the structure of crystalline matter built up by atoms which forms a periodic 3D lattice. The father and the son Bragg examined the diffraction of X-rays by a number of crystals and established the foundations of the field of crystallography.

Several processes describe interaction of X-rays and a matter: photoelectronic absorption, elastic and inelastic scattering. Also we should mention electron – positron pair production but it is suitable for irradiation with the energy starting from hundreds of keV – gamma rays. Since the current work is focused on X-rays in region 8 – 65 keV this effect can be neglected.

All these processes are commonly grouped to a number of effects: absorption, refraction, reflection and scattering [26].

1.1 Complex refractive index

A complex refractive index can be written as

$$n = 1 - \delta + i\beta \tag{1.1}$$

where the refraction is denoted by δ with the respect to the vacuum. In the energy range 10-20 keV it is positive value of the order 10^{-5}. The absorption is denoted by the imaginary part β and it is 3 orders of magnitude smaller than δ. Both can be derived by a complex atomic scattering factor - f [27]:

$$f = Z + f' + if'' \qquad (1.2)$$

$$\delta = \frac{N_a r_e \lambda^2 \rho}{2\pi A}(Z + f') \qquad (1.3)$$

$$\beta = \frac{N_a r_e \lambda^2 \varrho}{2\pi A} f'' \qquad (1.4)$$

where r_e is the classical electron radius, λ is the wavelength, N_a is Avogadro's number, Z is the number of the electrons in the element, ϱ is the density of the element and A is the atomic mass. Figure 1.1 shows how a wave traveling though the object with a complex refractive index n is attenuated and phase shifted relative to itself traveling in a vacuum. The intensity modification is described by the Lambert – Beer law:

$$I_2 = I_1 \exp(-\mu d) \qquad (1.5)$$

Here I_2 and I_1 are intensities of attenuated and primary waves respectively, μ is the linear absorption coefficient for the photon energy E and d is the material thickness. The absorption coefficient μ is related to the absorption index β and can be subdivided to the sum of number of contributions:

$$\mu = \frac{4\pi}{\lambda}\beta = \tau + \mu_R + \mu_C \qquad (1.6)$$

where τ, μ_R and μ_C are the absorption coefficients for the photoabsorption, for elastic and inelastic scattering respectively.

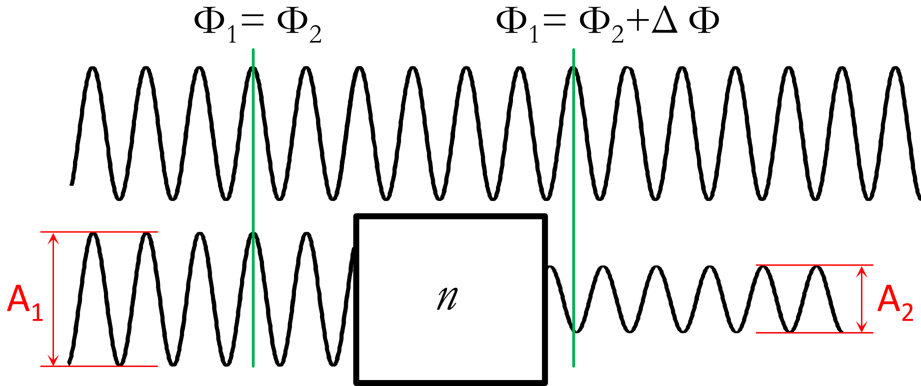

Figure 1.1. The result of the phase shift and attenuation of the wave travelled though the object with the refractive index *n*. The wave got a phase shift of ΔΦ relative to itself traveling in a vacuum and attenuated regarding to the Lambert – Beer law.

The phase shift of the wave $U(z,t) = A_2 \exp i(kz - \omega t - \Delta\Phi)$ transmitted thought the object with complex refractive index n is given by:

$$\Delta\Phi = \delta k d \tag{1.7}$$

where k is the wavenumber $k = 2\pi/\lambda$, d is the object thickness ω is the wave's angular frequency.

1.2 Refraction and reflection of X-rays

For X-rays matter is optically thinner than vacuum because the refractive index $n=1-\delta$ is slightly less than one. This result is in the fact that the phase velocity of X-rays is larger in the matter and the beam coming from vacuum (or air) is refracted away from the surface normal. Regarding to Snell's Law [28]:

$$n_V \sin\theta = n \sin\theta' \tag{1.8}$$

where θ and θ' are the angles between the surface normal and the incident ray and refracted ray respectively. In figure 1.2 is presented the difference in the refraction for visible light and X-rays.

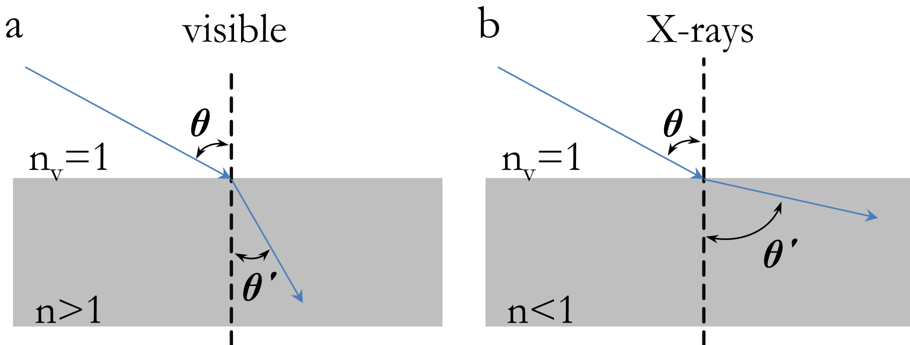

Figure 1.2. Refracted ray in case of visible light, the refraction coefficient is greater than 1, the refraction angle relative to the surface normal is smaller than incident – (a). Refraction for X-rays, the refracted angle is greater than incident one – (b).

In addition the refraction away from the surface normal implies that the total external reflection occurs when the incident angle is less than critical angle which denotes:

$$\theta_c = \sqrt{2\delta} \tag{1.9}$$

Taking into account that δ is in order of 10^{-5}, the critical angle is about number of milliradians.

1.3 Scattering of X-rays

X-ray scattering processes can be divided into two groups: elastic and inelastic. The elastic scattering is described by Rayleigh and called by his name. This type of scattering does not change the energy of the incident photon, it is only changing the direction of the propagation.

The most known consequence of Rayleigh scattering in X-ray physics is Bragg reflection, it is occurs with periodical structures with the period in the order of the incident wavelength.

Second important consequence is the small angle X-ray scattering, it is also the elastic scattering; it is occurred on inhomogeneities of macro-objects in the nm range. The recorded pattern contains information about the shape and the size of scatterers in the object. This type of scattering may be observed in the case of the reflection of X-rays by the surface. Let me introduce the well known Gaussian damping factor given by Rayleigh [29]:

$$R = |r_{12}|^2 \exp(-4k^2\theta^2\sigma^2) \tag{1.10}$$

where R is the reflection coefficient of the surface, θ is the angle the incidence and σ is rms (root mean square) roughness. It is widely used roughness correction to the Fresnel reflectivity $|r_{12}|^2$. It describes the loss of reflected intensity caused by the scattering on the surface roughness.

The Compton or inelastic scattering is the process which changes the energy of the incident photon. While X-ray photon collides with electron which located in the outer shell of the atom part of the energy transfers from the photon to the electron. The difference in energy results in a wavelength shift which can be described as:

$$\Delta\lambda = \frac{h}{m_0 c}(1-\cos\theta) \tag{1.11}$$

Here m_0 is the electron rest mass, c is the speed of light, h is the Planck constant, θ is the scattering angle.

2. Instrumentation

This dissertation is targeting on the design, characterization and application of interferometers at the ESRF undulator beamlines ID06 and ID11. In addition to synchrotron some of experiments are feasible to perform with the use of X-ray tube (mirror-based interferometers [30]). Therefore some information about X-ray sources is presented first. The general layout of the beamline is presented to provide the idea of the overall arrangement of beamline components, and of the dimensions of the beamline. Then the properties of the refractive optics for hard X-rays are presented. The refractive lenses acts as a device that generating a secondary source (as a part of interferometer).

2.1 X-ray sources

2.1.1 X-ray tube

The first X-ray tube was manufactured by Röntgen but it was not reliable. The new design was developed by W.D. Coolidge from the General Electric Research Laboratories in New York, where electrons were produced by glowing filament and metal anode which had a water cooling system (figure 2.1). The intensity of produced X-rays was limited by the efficiency of a cooling system. The maximum power of this device did not exceed 1 kW.

The rotating anode X-ray tube (figure 2.1) allowed to increase the total power by dissipating heat over a much larger volume than in standard tube. The most crucial problem of this type of tube is manufacturing of high vacuum seal on the rotating shaft, inside which the cooling water must flow.

The X-ray spectrum produced by the tube has two distinct components. The first is a continuous part caused by deceleration of electrons. This is known as *bremsstrahlung* radiation (from the German *bremsen* - brake). The maximum energy of this radiation corresponds to the high voltage applied to the tube.

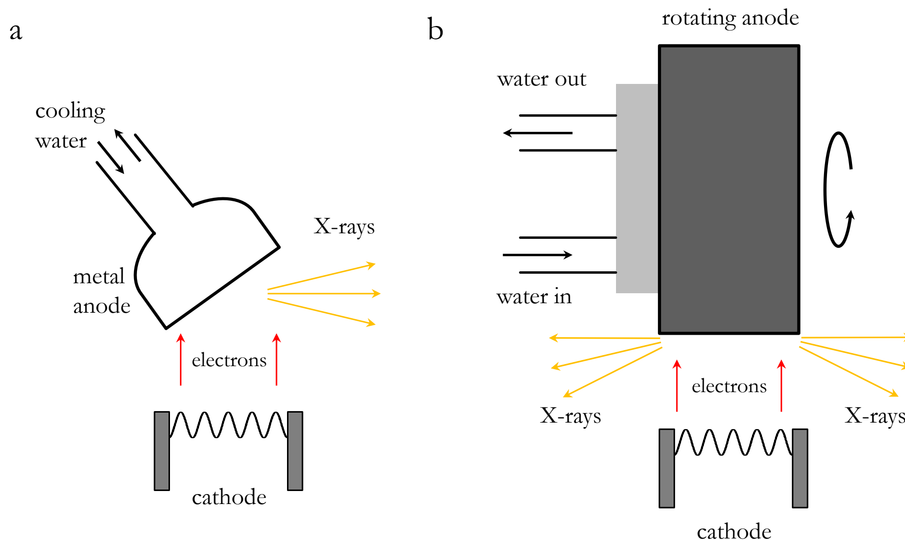

Figure 2.1. The standard X-ray tube with water cooling system – (a). X-ray tube with rotating anode – (b).

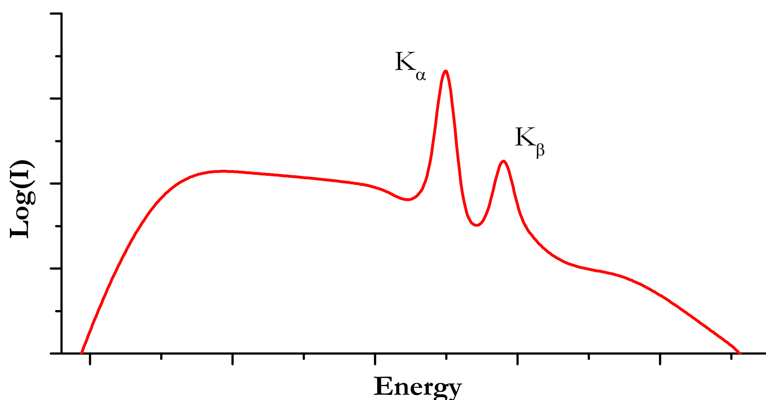

Figure 2.2. The spectrum of an X-ray tube

The second component is the emission spectrum of the material of the anode so-called fluorescent radiation. Usually for experiments requiring a monochromatic radiation one utilizes the K_α characteristic line which is well more intense than the *bremsstrahlung* spectrum. The schematic spectrum of X-ray tube is presented in figure 2.2.

Along with the spectrum there is another important parameter to characterize X-ray sources – brilliance. The brilliance is denotes as the number of photons per seconds in a given bandwidth of $\Delta E/E$ divided by the source size S and solid angle $\Delta\Omega$. Brilliance is used to compare X-ray sources quantitatively:

$$\text{Brilliance} = \frac{\text{photons/second}}{\Delta\Omega \times S \times \Delta E/E} \tag{2.1}$$

Nevertheless Brilliance does not contain any information about coherent properties of X-ray sources. The coherent properties of X-ray beam will be discussed in chapter 4.

2.1.2 Synchrotron

The advent of synchrotrons has opened a new chapter of the history of X-ray sources. There highly relativistic electrons circulate inside a storage ring with high level of vacuum and emit synchrotron radiation.

This effect was observed in accelerators for high energy particle physics and so-called spurious or parasitic radiation. It was found later that this type of radiation could have various applications. Nowadays many dedicated storage rings exists to produce synchrotron radiation. One of the synchrotrons with highest brilliance is the European Synchrotron Radiation Facility (ESRF). The experiments described in this wok were performed at the ESRF in Grenoble, France. The ESRF is the first 3rd generation synchrotron, it was inaugurated in 1994. Along with 3rd generation storage rings free electron laser (FEL) sources are being developed. These sources may be suggested as a next generation sources which generate several orders of magnitude more brilliant (in comparison with dedicated storage ring) and fully coherent beam. Figure 2.3 (a) shows the evolution of X-ray sources over the years.

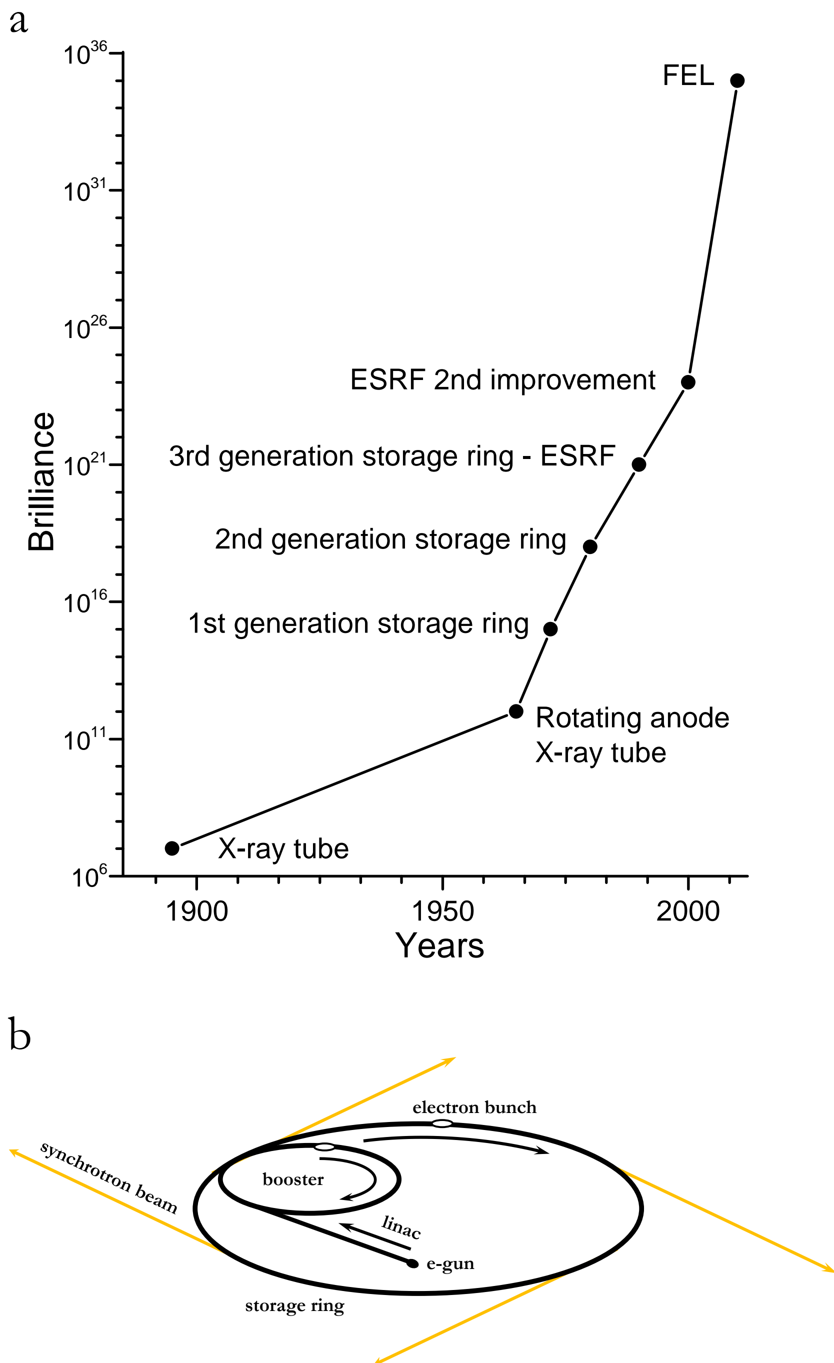

Figure 2.3. The evolution of X-ray sources – (a), schematic view of synchrotron – (b).

The layout of a synchrotron source is presented in figure 2.3 (b). Such sources consist of an injector where electrons are emitted and accelerated to energies about 200 MeV. A booster ring is used to increase the electron energy to a number of GeV. Then, the electrons are injected to a storage ring and they are kept on a closed orbit by bending magnets (BM). In addition to BM storage ring has quadrupoles and sextupoles allowing forming and focusing the electron beam. The 3rd generation storage ring also has a number of straight sections which allows to use insertion devices (ID) such as wigglers and undulators. Because the experiments presented in this work were performed with the undulator radiation I will not dwell on the bending magnet radiation.

2.1.2.1 Insertion devices

The insertion device consists of two rows of alternating magnets facing each other and creates a magnetic field with periodic structure. This magnetic field forces electrons onto an oscillating path. The optical properties of the insertion device may be characterized by the dimensionless parameter [26]:

$$K \equiv \frac{eB_0\lambda_u}{2\pi m_0 c} \tag{2.2}$$

where m_0 is the rest electron mass, c is the speed of light, e is the electron elemental charge, B_0 is the peak magnetic field of ID, λ_u is the ID period.

The maximum deflection angle of electrons is denotes by:

$$\alpha_{max} = \frac{K}{\gamma} \tag{2.3}$$

where γ is the Lorentz factor which is defined as:

$$\gamma = \frac{1}{\sqrt{1-\beta^2}}, \text{ with } \beta = \frac{v}{c} \tag{2.4}$$

where v is the speed of electrons in the storage ring. This allows to differentiate undulator and wiggler.

For wiggler $K \gg 1$ and $\alpha_{max} \gg 1/\gamma$. So the angle of the emission cone $1/\gamma$ of an electron is much smaller than maximum deflection angle. This

results in the fact that the emission processes of an electron at different parts of its oscillation path are independent from each other. In other words they are incoherent.

In the case of undulator $K \leq 1$ and $\alpha_{max} \leq 1/\gamma$. Then the emission cones from electron at different positions of its oscillation path overlap coherently. So it is not possible to distinguish which point of the electron path responsible for emitted photon. As the result the emitted beam intensity is proportional to the square of the number of periods of the undulator. This made undulators the most brilliant and coherent available sources. The photon energy of the beam produced by undulator may be varied by changing K with the gap of undulator. The wavelength of undulator beam is denotes by:

$$\lambda_{j} = \frac{\lambda_{u}}{2\gamma^{2} j}(1 + \frac{K^{2}}{2} + \gamma^{2}\theta^{2}) \qquad (2.5)$$

where θ is the viewing angle of the observer and j is the undulator harmonic.

An example of undulator spectra (for on axis observation) is presented in figure 2.4.

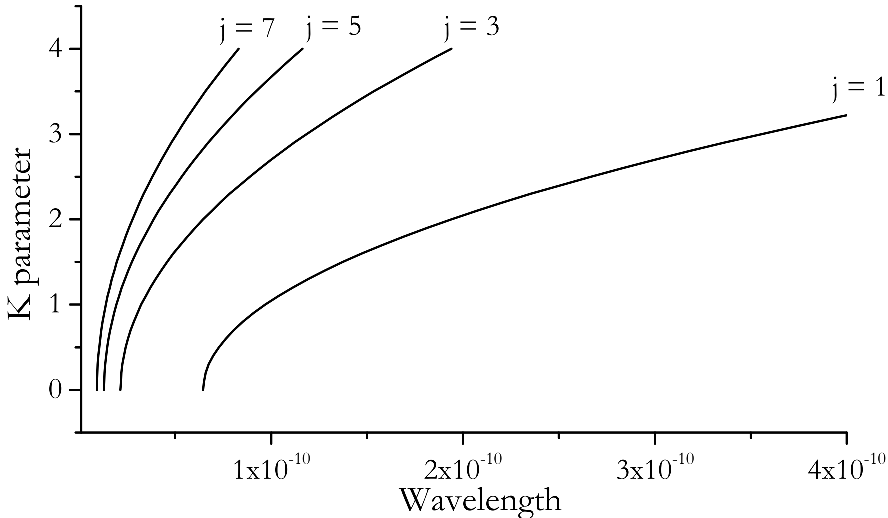

Figure 2.4. An undulator spectra.

2.1.2.2 Emittance and source size

The product of source size and divergence is known as the emittance of a source (or electron beam) [26]. For a synchrotron storage ring, the electron beam emittance parameter is constant along the orbit and along the ring, according to the Liouville's theorem.

Typical values for the electron beam parameters for straight section at the ESRF in the vertical direction are [31] σ_v = 8 μm, σ_v' = 3.2 μrad (for electron beam size and divergence respectively). Then the vertical emittance is $\varepsilon_v = \sigma_v\sigma_v'$ = 3 pm rad, therefore the declared value [31] is slightly greater – 4 pm.

The size of the photon source depends on the electron beam emittance [32]:

$$S = \sqrt{\varepsilon_v \beta_v (S)(1 + D_v (\frac{\Delta\lambda}{\lambda}))^2} \tag{2.6}$$

where β_v is a function related to transverse size of the electron beam at the location S, D_v is the dispersion. According to [32], due to small part which is under the square, the relation is possible to simplify: $S = \sqrt{\varepsilon_v \beta_v (S)}$. On the other hand it is known that the photon source size cannot be smaller than the value set by the diffraction limit. Beyond the diffraction limit any narrowing of the source size leads to the increase of the divergence and other way around. So the diffraction limited source size and angular divergence for the undulator denotes:

$$\sigma_v = \frac{\sqrt{\lambda N \lambda_u}}{4\pi} \qquad \sigma_v' = \sqrt{\frac{\lambda}{N\lambda_u}} \tag{2.7}$$

where N is the number of periods of the undulator.

All formulae presented here are valid also for horizontal values which are much larger and not relevant for this work.

2.1.2.3 A beamline layout

All experiments presented in this work have been performed at two undulator beamlines at the ESRF: ID06 and ID11. Figure 2.5 shows the schematic setup of the undulator beamline ID06.

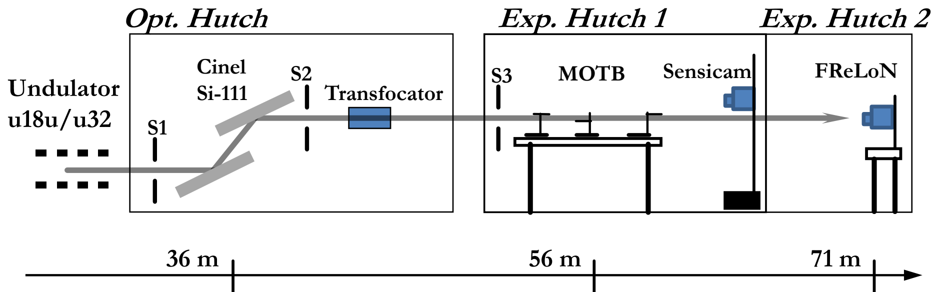

Figure 2.5. Schematic setup of the undulator beamline ID 06 at the ESRF.

The optics hutch contains primary (S1) and secondary (S2) slits. The monochromatization of the beam is performed by a fixed exit double crystal monochromator (Si (111)) in the energy range 8-30 keV. The interferometry experiments were performed on the micro optics test bench (MOTB) in the 1st experimental hutch. The interference patterns were recorded on the high resolution CCD cameras equipped with a fluorescence screen and an optical objective allowing to reach up to 1 μm of the spatial resolution. The observation distance is limited by the length of the beamline and equals to 15 meters.

The ID11 beamline differs from ID06; it was designed especially for the high energies of X-rays. The monochromatization of the incoming X-rays was performed by the double bent-crystal monochromator operating in a horizontal Laue geometry in the energy range 18 keV – 140 keV. Compared to flat crystals in Bragg geometry, asymmetrically cut bent crystals deliver up to 10 times higher photon flux, particularly at higher energies. The horizontal geometry allows direct crystal cooling via contact with a thermally controlled InGa bath. Attenuators upstream from the monochromator remove essentially all flux below 25 keV; this, coupled with the Laue geometry, means that the thermal load is small and such cooling is sufficient. Consequently, the monochromator is very stable, needing no adjustment or feedback after alignment. The horizontal geometry also minimizes the perturbation of the vertical source size.

The total length of the beamline allows to observe interference patterns at the distance of 50 m from an interferometer and up to 100 m from the source.

2.2 The refractive lenses for X-rays

The low value of δ for X-rays made it difficult to fabricate refractive lenses. This is why the discoverer of this "kind of radiation" reasonably declared that lenses for X-rays are not feasible. Nevertheless in 1996 [18] the first compound refractive lens (CRL) was produced. Because the value of δ is very low, to achieve reasonable focal distance, stacks of lenses should be used. The first CRL consisted of number of cylindrical holes (because δ for X-rays slightly greater than 0) drilled in a piece of Aluminum. The large number of holes allowed to obtain short focal distance in the energy range 5-40 keV. This CRL generates the focus of the line shape showing strong aberrations (spherical) caused by the circular profile of the holes.

To avoid spherical aberrations the lens profile should be parabolic. All lenses in this work have parabolic shape so I will not dwell on circular lenses and its defects.

The material for CRL manufacturing has a significant influence on the optical performance of the lens. The strength of the refraction is described by the refractive index decrement δ which typically is in the order of 10^{-6} at energies 10-20 keV. The imaginary part β of the refractive index is represents the absorption and is in the order of 10^{-9} in the same energy range.

It is clear that all materials have a weak refraction and relatively high absorption. Thus elements with low absorption (low – Z elements) are more suitable for lens manufacturing. At the moment CRL are producing from Be, Al, Si, Ni and Carbon based materials.

Since their development, the use of X-ray refractive lenses has rapidly expanded to the extent that they are now widely used on synchrotron beamlines [18, 33-35]. Being in-line optics, the compound refractive lenses offer a number of advantages, they are easy to align, relatively insensitive to misorientations and mechanical vibrations and stable even in the white beam [36]. The use of tunable systems such as transfocators with a variable number of lenses, offers focal length tunability that drastically extends the applicability of refractive optics [37]. They can be adapted to very high X-ray energies by modifying composition and number of lenses, and furthermore, refractive optics can be easily inserted and removed from the beam to allow fast switching of the beam size from the micrometer to nanometer scale.

The field of applications of refractive optics is not only limited to beam conditioning, but can be extended into the area of Fourier optics, as well as coherent diffraction and imaging techniques [38]. Using the intrinsic

property of the refractive lens as a Fourier transformer, coherent diffraction microscopy and high resolution diffraction methods have been proposed to study 3D structures of semiconductor crystals and mesoscopic materials [39-41].

2.2.1 Focal length

The focal length of single double concave lens is denotes:

$$F = \frac{R}{2\delta} \tag{2.8}$$

where R is the curvature radius of the parabolic shape of the lens and F is the lens focal length.

It was shown form the exact theory [42] that CRL can be considered as a thin lens while the total length of CRL is more than 3 times smaller than the focal length. Thus the focal length of a CRL consisting of N single double concave lens is given by [43]:

$$F = \frac{R}{2N\delta} \tag{2.9}$$

Since δ depends on the energy ($\delta \sim E^{-2}$) the focal length is varying as the square of the energy i.e., X-ray lenses are highly chromatic.

2.2.2 Transmission and effective aperture of the lens

For the X-ray lenses it is possible to mention 2 types of aperture (see figure 2.6): the geometrical aperture and the effective aperture. The geometrical aperture (or physical aperture) is the size of the lens $A_{\text{phys}} = 2R_0$. The effective aperture is usually smaller than geometrical aperture because the part of the beam transmitted through lens is absorbed by the material.

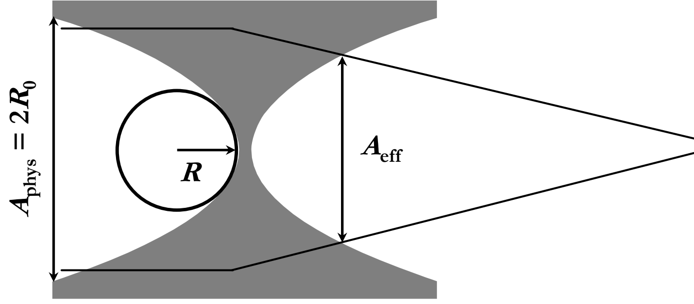

Figure 2.6. The schematic view of single parabolic X-ray lens.

For the thin lens approximation [42] the effective aperture is denotes as [43]:

$$A_{\text{eff}} = 2R_0\sqrt{\frac{1-\exp(-a_{\text{p}})}{a_{\text{p}}}} \tag{2.10}$$

The transmission of a lens T gives the fraction of photons that are transmitted through the lens. It can be derived by integrating Lambert – Beer's law over the lens physical aperture [43]:

$$T = \frac{\exp(-\mu N d)}{2a_{\text{p}}}(1-\exp(-2a_{\text{p}})) \tag{2.11}$$

where d is the minimal thickness between parabola apexes and a_{p} is the factor responsible for attenuation inside the lenses and for scattering on roughnesses of lenses surfaces [43]:

$$a_{\text{p}} = \frac{\mu N R_0^2}{2R} + \frac{N\delta^2\sigma^2 R_0^2 k^2}{R^2} \tag{2.12}$$

where σ is rms surface roughness of the lens.

If a_{p} is small and the lens surface roughness can be neglected, the effective aperture can be rewritten as:

$$A_{\text{eff}} = 2\sqrt{\frac{2R}{\mu N}} \tag{2.13}$$

The numerical aperture N.A. is directly depends on the effective aperture [43]:

$$\mathrm{N.A.} = \frac{A_{\mathrm{eff}}}{2z} \tag{2.14}$$

where z is the distance between lens and object.

The lateral resolution r, of the CRL, is defined by the numerical aperture [43]:

$$r = 0.75 \frac{\lambda}{2\mathrm{N.A.}} \tag{2.15}$$

2.2.3 Depth of field and depth of focus

The depth of field of the refractive lens is defined as the distance along the optical axes between 2 objects which can be correctly imaged and can be written as [43]:

$$d_z = \frac{8\lambda z}{\pi A_{\mathrm{eff}}^2} = \frac{2\lambda}{\pi (\mathrm{N.A.})^2} \tag{2.16}$$

A microbeam size along the optical axes may be characterized by the depth of focus parameter (DoF) which is defined as the distance where the lateral beam size is smaller than $B_v\sqrt{2}$ [44]:

$$\mathrm{DoF} = \frac{2 z_1 B_v}{A_{\mathrm{eff}} \sqrt{2 \ln 2}} \tag{2.17}$$

where z_1 is the lens imaging distance and B_v is a lateral size of the focal spot.

2.3. Si planar structures manufacturing

In this chapter I focus on manufacturing of planar structures from Si crystals. The main manufacturing steps are electron beam lithography and deep reactive ion plasma etching. To understand each manufacturing step as well as the whole process the following chapter gives an overview of these technologies.

2.3.1 Electron beam lithography

The lithography processes used in micromachining and microfabrication are based on selective removing of parts of a resist layer and subsequent etching. Electron beam lithography (e-beam lithography) is a precise technique used to create structures down to the nanometer scale into layers of resist. The primary advantage of this technique is that its resolution is up to few nanometers. A collimated beam of electrons is scanned across the surface of a sample (in my case it is Si crystal) which is covered by an electron sensitive film called resist. Following the illumination of the crystal, the structures are treated in a solvent (this process so-called developing). During that process the illuminated parts of the pattern are removed (positive resist) or all non exposed parts of the layer are lifted (negative resist).

A typical design of an electron beam lithography setup is presented in figure 2.7. This set-up is very similar to a scanning electron microscope. Such systems for purposes of commercial applications are very expensive (more than 1 million of US dollars). For scientific research applications it is very common to modify a scanning electron microscope (SEM) to an e-beam lithography system using relatively low cost parts (around 100 thousands US dollars).

The electrons are emitted by filament under the heating. To achieve high resolution, the electrons have to be focused by magnetic lenses. This focused beam is scanned across the surface of the Si crystal by deflection magnets or by electrostatic fields of the condenser. The minimal feature size that can be created by e-beam lithography is limited by a number of different factors, e.g., acceleration voltage, beam spot size, type of resist and its thickness. One physical limitation of the minimal size of the feature is the interaction between electrons and matter. At the moment then the

electrons collide with the resist many scattering events take place which lead to the broadening of the initial beam spot size. At the same time electrons penetrate through the resist where additional scattering occurs. Features that have border with many other structures receive higher doses than features without neighbors. This effect is called the proximity effect and has to be taken into account and corrected in order to maintain tight size control of the feature.

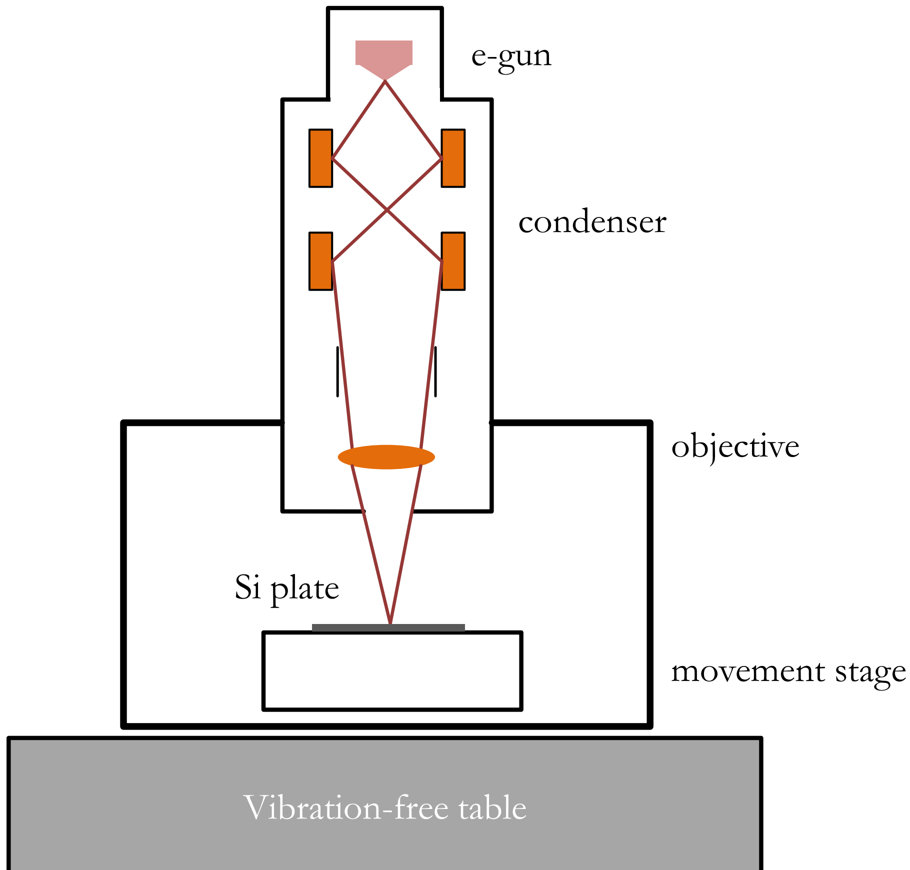

Figure 2.7 Schematic view of typical e-beam lithography set-up.

2.3.2 Deep dry etching

At the moment dry etching techniques play a significant role in micromachining and microfabrication technologies. The main advantage (in comparison with wet etching) is the close control of the parameters of the process and as the result the better reproducibility of the etching process.

Etching process can be isotopic (uniformly distributed in all directions) or anisotropic (it goes in one direction).

Two distinct dry etching techniques may be highlighted: plasma and ion etching. Plasma etching uses free radicals formed in plasma. These radicals react with the matter to be etched and forms volatile compounds, which can be swept away with the gas flow. The reactive species are transported to the substrate by diffusion or by convection. Plasma etching has a chemical character and is uniformly distributed in all directions (isotopic etching).

The ion etching process is based on ion sputtering effect. A noble gas is ionized inside a reaction chamber and accelerated towards the sample by an electrostatic field. Accelerated ions hit into the surface of the sample and strike atoms of the material to be etched. This etching process has a highly anisotropic character.

A combination of both techniques is called reactive ion etching (RIE). This process uses highly reactive ionized gases (plasma) containing ions, free electrons and free radicals. This plasma is characterized by its relatively low temperature (50 – 300 °C), low pressure (10 – 400 Pa) and low flow rates (50 – 500 cm^3/min). By using an adequate etching gas it is possible to combine the advantages of plasma etching (selectivity) and ion etching (anisotropic process).

The etching of the structures with high aspect ratio (the ratio of the depth of the feature to the feature lateral size) is a big challenge. Large depths of the etching mean difficulties with stable etch conditions during the whole process. Some effects and problems (such as mask erosion, mask undercutting, bottling and RIE lag) may appear. Many of the problems can be overcome by a precise adjustment of the etching parameters and sidewalls passivation. In passivation process the sample is coated by thin layer to protect the sidewalls from further etching.

The BOSCH process is based on step by step variation of passivation and etching processes. This process overcomes most of the problems related to the etching of structures with high aspect ratio. Deep Si etching by BOSCH process leads to scalloping (see figure 2.8) appearance from alternated etching and passivation processes.

Optimizing the BOSCH process compensating of the mask undercut and its step, the planar interferometers with vertical sidewalls and up to 70 μm in depth were manufactured within the framework of current work. C_4F_8 and SF_6 were used as the passivation and etch gasses respectively during the BOSCH process.

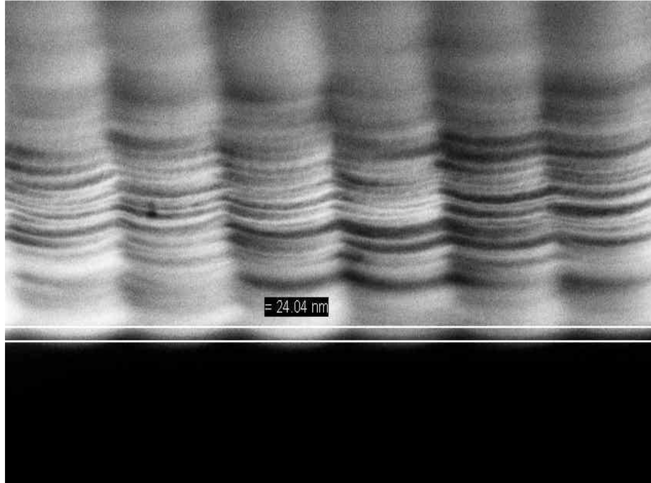

Figure 2.8 An example of scalloping.

3. Diffraction

The term diffraction has been defined as “any deviation of light rays from rectilinear paths which cannot be interpreted as reflection or refraction” by Sommerfeld [6].

3.1 The Fresnel-Kirchhoff diffraction formula

The solution of the problem of the diffraction requires consider the Huygens principle of propagation of the light: every point in the wavefront acts as a secondary source of spherical waves. The shape of the wavefront is given by the superposition of all spherical waves.

Let me introduce the hole in the not transparent screen so-called aperture which has the next properties:

1. Across the aperture surface - Σ, the field distribution U and its derivative are exactly the same as they would be in the case of absence of the screen.
2. Outside the aperture, in the geometrical shadow of the screen, the field distribution U and its derivative are identically zero.

This aperture is illuminated by single spherical wave,

$$U(P_1) = \frac{A\exp(ikr_{21})}{r_{21}} \tag{3.1}$$

This wave are raised from a point source at P_2 at a distance r_{21} from P_1, see figure 3.1.

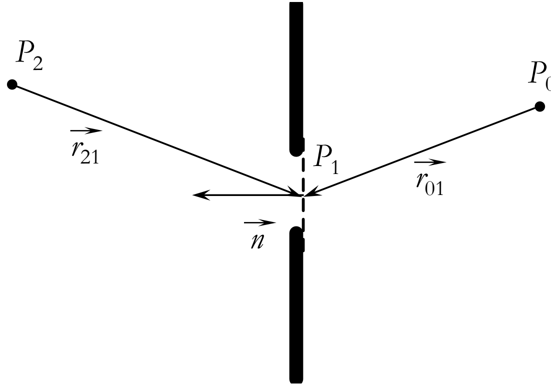

Figure 3.1. Point source illumination of a plane screen with aperture.

If r_{21} is big enough (many wavelengths) then the field distribution in point P_0 denotes [8]:

$$U(P_0) = \frac{A}{i\lambda} \iint_{\Sigma} \frac{\exp\left[ik(r_{21} + r_{01})\right]}{r_{21} r_{01}} \left[\frac{\cos(\vec{n}, \vec{r}_{01}) - \cos(\vec{n}, \vec{r}_{21})}{2} \right] ds \qquad (3.2)$$

3.2 Fresnel diffraction

Assuming that the dimensions of the object are large in comparison with the wavelength and small in comparison with distances r_{21} and r_{01}, the deflection angles is small so paraxial approximation for (3.2) is introduced as [45]:

$$r_{01} \approx z + \frac{(x-\xi)^2 + (y-\eta)^2}{2z} \tag{3.3}$$

where ξ and η are coordinates in the diffraction geometry in figure 3.2 and z is the observation distance.

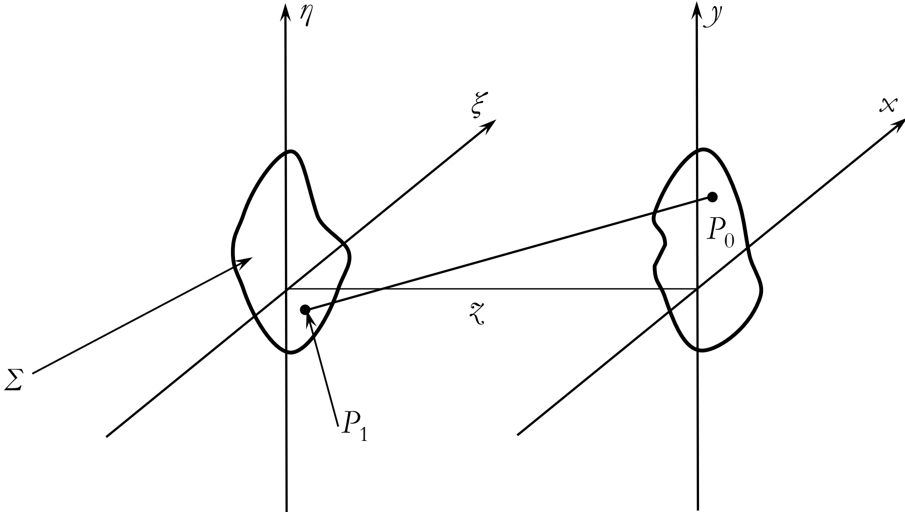

Figure 3.2. Diffraction geometry.

The resulting expression for the field at (x,y) coordinate system becomes:

$$U(x,y) = \frac{\exp(ikz)}{i\lambda z} \iint U(\xi,\eta) \exp\left[\frac{ik}{2z} \left[(x-\xi)^2 + (y-\eta)^2 \right] \right] d\xi d\eta \tag{3.4}$$

This equation is the Fresnel diffraction integral. The equation (3.4) may be presented as a convolution in the form [8]:

$$U(x,y) = \iint U(\xi,\eta) h(x-\xi, y-\eta) d\xi d\eta \tag{3.5}$$

with the convolution kernel:

$$h(x,y)=\frac{\exp(ikz)}{i\lambda z}\exp\left[\frac{ik}{2z}(x^2+y^2)\right] \tag{3.6}$$

The Fourier transform is found if the term $\exp\left[\frac{ik}{2z}(x^2+y^2)\right]$ is factored outside the integral signs [8]:

$$U(x,y)=\frac{\exp(ikz)}{i\lambda z}\exp\left[\frac{ik}{2z}(x^2+y^2)\right]\iint U(\xi,\eta)\times$$
$$\exp\left[\frac{ik}{2z}\left[\xi^2+\eta^2\right]\right]\exp\left[\frac{-2\pi i}{\lambda z}\left[x\xi+y\eta\right]\right]d\xi d\eta \tag{3.7}$$

3.3 Fraunhofer diffraction

The Fresnel – Kirchhoff diffraction formula describes Fraunhofer diffraction in terms of far field approximation:

$$z \gg \frac{k(\xi^2 + \eta^2)_{\max}}{2} \tag{3.8}$$

In the region of Fraunhofer diffraction (or far field) the field distribution denotes [8]:

$$U(x,y) = \frac{\exp(ikz)}{i\lambda z} \exp\left[\frac{ik}{2z}(x^2 + y^2)\right] \iint U(\xi,\eta) \times \exp\left[\frac{-2\pi i}{\lambda z}\left[x\xi + y\eta\right]\right] d\xi d\eta \tag{3.9}$$

The far field condition may be rewritten in the terms of the object size D:

$$z \gg \frac{2D^2}{\lambda} \tag{3.10}$$

Another way to satisfy far field condition has been expressed by J.W. Goodman[8]:

"In addition, Fraunhofer diffraction patterns can be observed at distances much closer than implied by relation (3.10) provided the aperture is illuminated by a spherical wave converging toward the observer, or if a positive lens is properly situated between the observer and the aperture."

So I will demonstrate this on the example of the positive lens. The phase transformation performed by lens can be written as [8]:

$$t_l(\xi,\eta) = \exp\left[-i\frac{k}{2f}(\xi^2 + \eta^2)\right] \tag{3.11}$$

Let's consider the case when the object located against the lens, because this case presented in the experimental part of this thesis. Then the amplitude distribution behind the lens using (3.11) will be:

$$U'(\xi,\eta) = U\ (\xi,\eta)P(\xi,\eta)\exp\left[-i\frac{k}{2f}(\xi^2+\eta^2)\right] \tag{3.12}$$

where $U(\xi, \eta)$ is the input monochromatic wave incident on the lens and $P(\xi, \eta)$ is the lens pupil function.

To find the distribution $U_f\,(x,y)$ in the back focal plane of the lens, the Fresnel diffraction formula (3.7) is applied. Replacing $z = f$ and assuming that lens aperture is bigger than the physical extent of the input, then the distribution in the focal plane will be [8]:

$$U_f(x,y) = \frac{1}{i\lambda f}\exp\left[\frac{ik}{2f}(x^2+y^2)\right]\iint U(\xi,\eta)\times \exp\left[\frac{-2\pi i}{\lambda f}[x\xi + y\eta]\right]d\xi d\eta \tag{3.13}$$

It is easy to see that the complex amplitude distribution of the field in the lens focal plane is the Fraunhofer diffraction pattern of the field incident on the lens (3.9) but without quadratic phase factor that precedes the integral. In most cases the real interest is the intensity across the focal plane. The phase term is important to calculate another field distribution after further propagation. In the case of the real experiment, the intensity distribution will be measured.

3.4 Diffraction on periodical objects – Talbot effect

It is known since 1836 [46] that under monochromatic illumination a periodical object can be self reproduced at a certain distance, known as the Talbot distance. This so-called the Talbot effect was explained by Lord Rayleigh in 1881[4]. To demonstrate this effect Talbot used a grating and visible light:

"About ten or twenty feet from the radiant point, I placed in the path of the ray an equidistant grating made by Fraunhofer, with its lines vertical. I then viewed the light which had passed through this grating with a lens of considerable magnifying power. The appearance was very curious, being a regular alternation of numerous lines or bands of red and green color, having their direction parallel to the lines of the grating. On removing the lens a little further from the grating, the bands gradually changed their colors, and became alternately blue and yellow. When the lens was a little more removed, the bands again became red and green. And this change continued to take place for an indefinite number of times, as the distance between the lens and grating increased. In all cases the bands exhibited two complementary colors. It was very curious to observe that though the grating was greatly out of the focus of the lens, yet the appearance of the bands was perfectly distinct and well defined." [46]

In the general case when the point source located on the finite distance z from the periodical object with the transmission function *T(x)* the field amplitude at the distance z_n can be written as [45]:

$$A(x_0) = C\int \exp(\frac{ikx_1^2}{2z_n})T(x_1)\exp(\frac{-ik(x_0 - x_1)^2}{2z})dx_1 \qquad (3.14)$$

Talbot image (so-called fundamental) will appear at distance z_T:

$$\frac{1}{z} + \frac{1}{z_T} = \frac{\lambda}{d^2} \qquad (3.15)$$

where d is the period of the object

It was shown [47-49] that there is an infinite family of Talbot images between the object and fundamental image. The fractional Talbot distances are $z_{pq} = pz_T/q$, where p and q are integers, and $p < q$. However, the main set of distances is $z_n = z_T/n$, where $n = 1, 2,...$.

The Talbot imaging approach was already applied at hard X-rays in which a single Fresnel diffraction image of a grating was obtained with a microfocus X-ray generator in reflection geometry. Fractional Talbot imaging of the phase grating at reduced defocusing distances were used for coherence characterization and phase modulation of the object, as well as grating interferometer for phase contrast imaging [22, 50, 51]. Recently, Talbot imaging was also used for electrochemical photolithography of Ni under coherent X-ray irradiation [52].

4. Interference with partially coherent light

Interference is the phenomenon resulting from superposition of correlated waves.

4.1 Coherence

Before this chapter I considered the beam to be monochromatic and fully coherent, so there were no any shifts of the phase on the surface of the wavefront. But this case is only suitable for the ideal monochromatic point source, unfortunately for real sources the spectral bandwidth and size of the source have to be taken into account. We should mention two types of coherence, a temporal coherence and a spatial coherence. The temporal coherence may be considered as the ability of a light beam to interfere with a delayed version of itself. It arises from consideration of the finite spectral bandwidth. The spatial coherence is the ability of a beam to interfere with a spatially shifted version of itself. It is directly characterized by the angular source size.

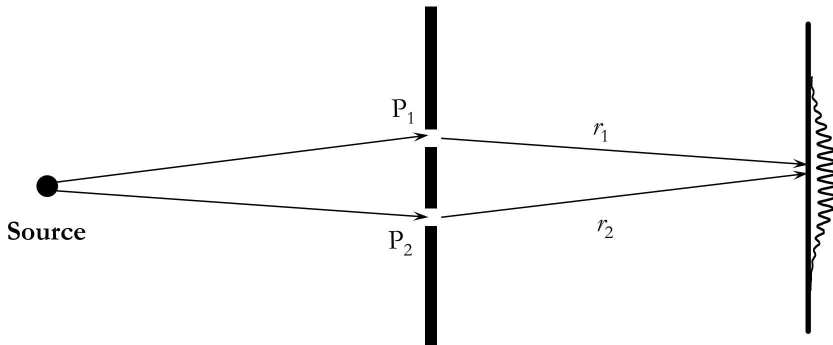

Figure 4.1. Interference geometry.

4.1.2 Mutual coherence function

The field *U(x)* used in previous chapter does not contain information about coherent properties of the light. The concept of mutual coherence function is followed from both spatial and temporal shifting [53, 54]:

$$\Gamma(r_1, r_2, \tau) = \langle U^*(r_1, t) U(r_2, t+\tau) \rangle = \\ = \lim_{t\to\infty} \frac{1}{2t} \int_{-t}^{t} U^*(r_1, t) U(r_2, t+\tau) \mathrm{d}t \tag{4.1}$$

where Γ is a spatial and temporal cross-correlation function of the time dependent field also called mutual coherence function between the points P_1 and P_2 (see figure 4.1), *t* and τ are the time and the time interval between beams from points P_1 and P_2.

The normalized mutual coherence function called complex degree of coherence of the light at the points P_1 and P_2:

$$\gamma(r_1, r_2, \tau) = \frac{\Gamma(r_1, r_2, \tau)}{\sqrt{I(r_1) I(r_2)}} \tag{4.2}$$

where $I(r_1) = |U(r_1)|^2$ and $I(r_2) = |U(r_2)|^2$ are intensities at the observation plane from points P_1 and P_2 respectively. It indicates the correlation of the field between points P_1 and P_2 in case of waves from these points reach the observer with a path difference of $c\tau$. If $\gamma=1$ it means perfect correlation, $\gamma=0$ means no correlation and as the result no interference at the observer's position.

4.1.3 Temporal coherence

Consider the point source emits light in the form of wavepackets of length λ with bandwidth $\Delta\lambda$. Over the length of the wavepacket beam is assumed to be coherent. The maximum optical path difference between interfered beams which allows registering interference fringes called the longitudinal coherent length. It is denotes by:

$$l_l \approx \frac{\lambda^2}{\Delta\lambda} \tag{4.3}$$

4.1.4 Transversal coherence

To consider the longitudinal coherence I assumed that the source emitted the radiation was a point source. In practice the size of the real source has to be taken into consideration. Firstly let me consider an extended quasi monochromatic source emitting the radiation and two pinholes which are illuminated by this radiation (Young interferometer).

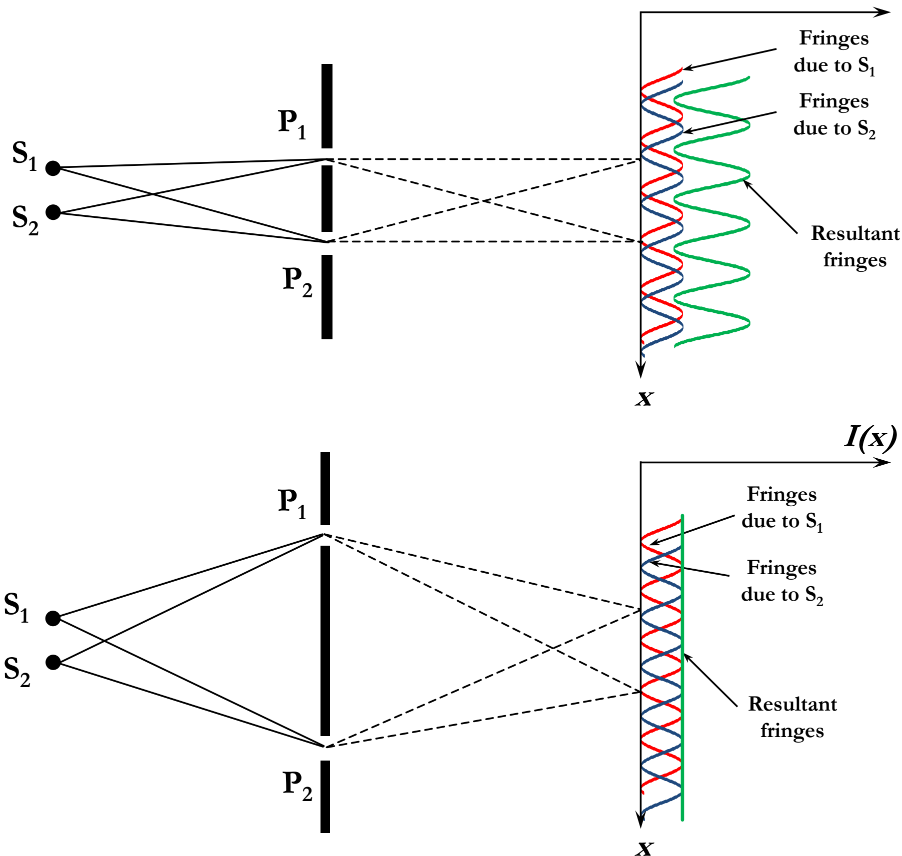

Figure 4.2. Physical explanation for the loss of the fringe visibility at large separation of pinholes: (top) small separation, (bottom) large separation

For simplicity, I will consider only two extreme points of this extended source – S_1 and S_2. Figure 4.2 illustrates the set-up. Two pin holes can be considered as secondary sources. In the case of the perfect correlation between P_1 and P_2 the interference pattern has a maximum fringe visibility. I define the visibility the same way as Michelson:

$$V \cong \frac{I_{\max} - I_{\min}}{I_{\max} + I_{\min}} \tag{4.4}$$

where $I_{\max}$ and $I_{\min}$ are intensities at the maximum and minimum of the fringe pattern. The pinhole separation corresponds to the situation with zero fringe visibility called spatial coherent length.

There is another way to explain the character of the observed fringes. If the light originates from a single point source, sinusoidal fringes of high (maximum) visibility are observed at the observer plane. Then, if the second point source radiating independently is added, a second fringe pattern is generated. It is the same period fringe pattern, but the position of this pattern is shifted relative to the first pattern.

If the separation of the pinholes is small the shift of the fringes of the one pattern relative to another is a negligible fraction of a period. If the separation is large the fringe pattern is shifted by a significant fraction of its period (or even many periods). The two fringe patterns may then practically cancel resulting in a loss of visibility. The increase of the size of the source (e.g. the distance between extreme points on the source) also led to the loss of visibility.

The spatial coherence length denotes by:

$$l_{\mathrm{coh}} = \frac{\lambda S}{z_0} \tag{4.5}$$

where S is the source size, z_0 is the distance from the source.

4.2 X-ray interferometry

While coherent radiation has been available and widely utilized in the region of visible wavelengths for a long time [3, 53, 55], it is just becoming available for X-rays [10, 12, 56, 57]. Coherent radiation in X-ray region is available due to advent of undulator radiation at synchrotron facilities [9, 11, 13, 14, 58]. Here I will make a review of interferometers has been implemented in X-ray region.

4.2.1 Bonse – Hart interferometer

The first interferometer in the X-ray region has been created by U. Bonse and M. Hart in 1965 [59]. This interferometer has an advantage in comparison with other X-ray interferometers: there are no strict requirements for coherence of the X-ray beam. The interferometer is made from a large and perfect crystal. By cutting two trenches into the block, different parts of the same crystal can act as a beam splitter, mirrors and analyzer (see figure 4.3). All three paths of the crystals have to be sufficiently thick to avoid passing the primary beam.

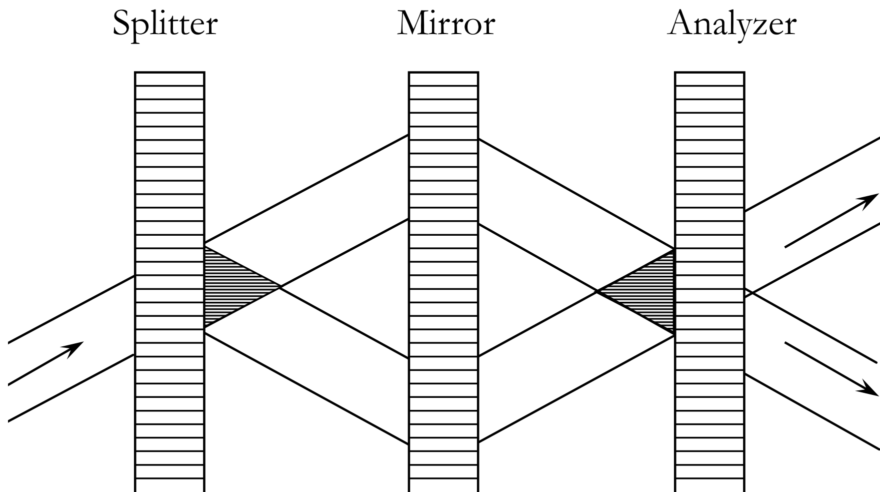

Figure 4.3. Schematic diagram showing interferometer operation.

The incident radiation is divided in two mutually coherent beams by means of symmetrical Laue diffraction in the beam splitter. Then these beams diffract again, converge and overlap on the entrance surface of the

analyzer. As the result they generate an interference pattern, the form of which depends on the difference of optical path between diffracted beams (analyzer and splitter have to be equidistant from mirror). However, the fringe spacing of this interference pattern is equal to the spacing of the Bragg planes which is difficult to observe directly. This difficulty is overcome by the use of the analyzer. Authors mentioned possible applications of this interferometer: the exact measurement of the refractive index of the sample inserted in one of two diffracted beams, exact measurements of the thickness of small objects, x-ray phase contrast imaging, measurements of extremely small lattice distortions and the direct measurements of dispersion surfaces.

4.2.2 Double slit interferometer

The classical Young double slit interferometer [3] has been performed for hard X-rays to quantitative measure the coherence properties of the radiation and to determine the index of the refraction [21].

The set-up was performed using a motorized slit with horizontally oriented tungsten blades with polished surface. The slit has been closed down to have a gap of 40 μm. Then, the gap has been splitted into two equal parts by placing a 30 μm thick tantalum plate parallel to the slit at the distance 3.5 cm upstream on the separated motorized stage. Figure 4.4 shows a sketch of the experimental set-up.

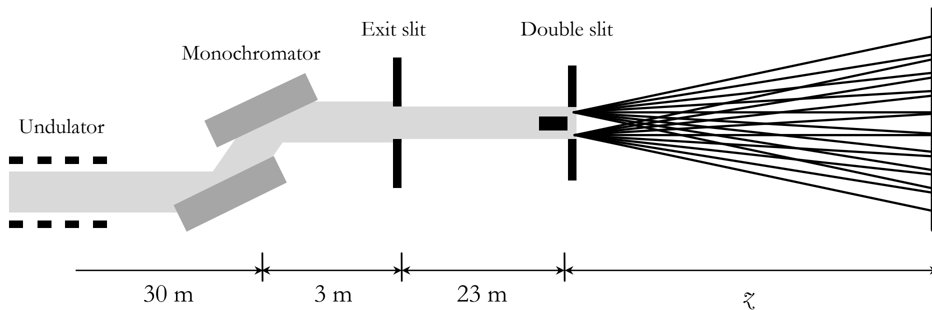

Figure 4.4. Experimental set-up for the double slit interferometer.

The intensity distribution at the distance z behind the double slits is given by [54, 60]:

$$I(x) = I_0 \left[\sin(k_d x) \big/ k_d x \right]^2 \left[1 + V\cos(k_D x) \right] + I_b,$$
$$k_D = \frac{2\pi D}{\lambda z},\ k_d = \frac{2\pi d}{\lambda z}, V = \frac{\sin(\pi SD/\lambda z_0)}{(\pi SD/\lambda z_0)} \tag{4.6}$$

where D is the gap between slits, S is the source size, d is the size of the slit, z is the interference pattern observation distance, z_0 is the distance from the source to the interferometer, I_b is the background intensity.

To measure the refractive index a small plate of Si was placed in front of one slit upstream of the interferometer. The refractive index was determined from the interference fringe shift relative to fringes without sample.

4.2.3 Double mirror interferometer

For hard X-rays it is more convenient to use reflecting optics because it is not easy to achieve thick slits with a short distance between them and because the edges of the slits reflect and add spurious radiation to the interference pattern. The main advantage of reflecting geometry is that under the grazing incidence angles mirror may be suggested as a narrow slit with the width as a function of the angle of the reflection (see figure 4.5).

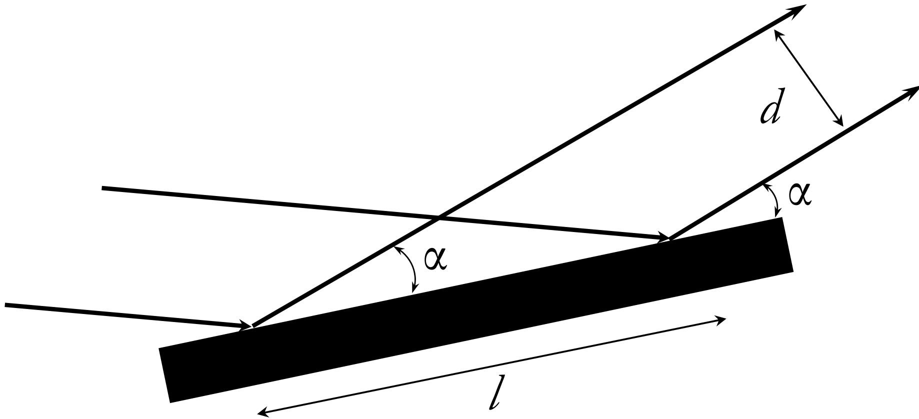

Figure 4.5. The oversight demonstration of the advantage of the reflecting geometry.

In this case the projection of mirror d denotes:

$$d = l\sin(\alpha) \tag{4.7}$$

The first x-ray interferometer based on the reflection, known as a bi-mirror, consisted of two independent sequential Si crystals placed on a goniometer [56]. This setup was used at grazing incidence angles below the critical angle of the total external reflection. The advantage of such technique is that the projected length of the mirrors to the observation plane is very small, making it equivalent to the Young's interferometer with narrow slits of micrometer size. Thus the interference patterns can be treated the same way as previous interferometer by taking into account the slit width from the equation (4.7).

The sketch of the principal scheme set-up is presented in figure 4.6.

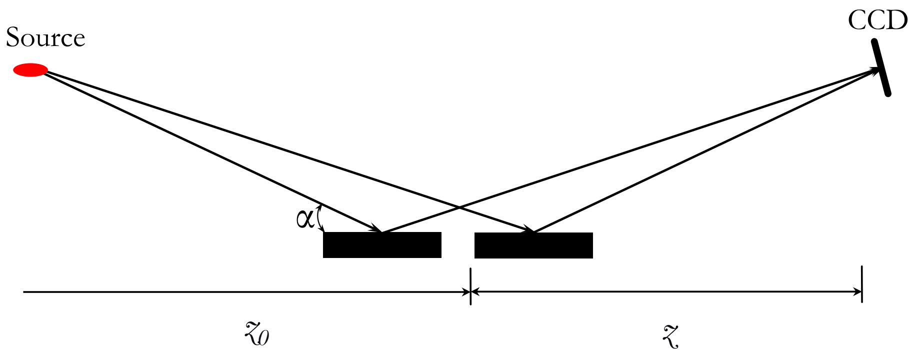

Figure 4.6. The double mirror experimental set-up.

4.2.4 Bilens interferometer

In order to use advantage of forming secondary source by CRL a bilens interferometer [24] has been designed and manufactured. It consists of two identical, parallel CRLs separated transversally by a distance. Each lens focuses the beam at the source imaging distance $z_F = F/(1-F/z_0)$, where F is the lens focal distance and z_0 is the distance from the source to the CRL. Then at some distance the cones from these sources overlap and in the region of overlapping occurs interference pattern. This scheme is also similar to the Young's double slit interferometer with narrow slits. The interferometer has been manufactured using a process involving electron beam lithography and deep reactive ion etching into silicon which I will describe later (in chapter 6). The principal experimental scheme is presented in figure 4.7.

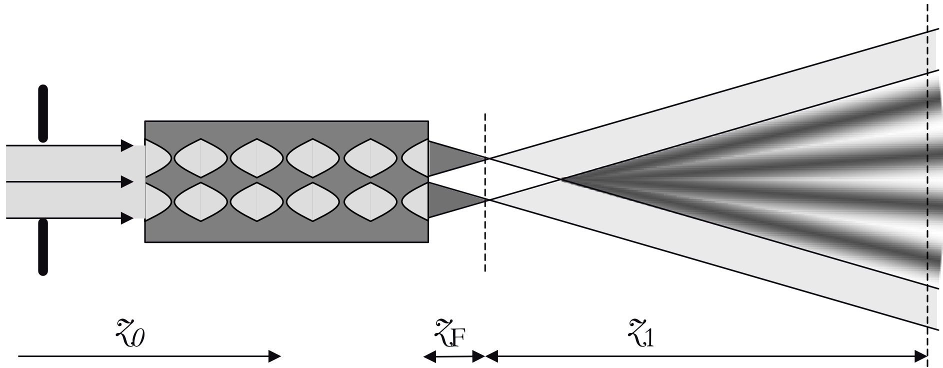

Figure 4.7. The bilens experimental set-up.

Similarly to the Young's interferometer the source size may be characterized quantitatively from the fringe visibility [24]:

$$S = \frac{\Lambda z_0}{(z_F + z_1)} \sqrt{-\frac{\ln V}{3.56}} \quad (4.8)$$

where Λ is the fringe spacing and z_1 is the interference pattern observation distance.

4.3 The study of coherence of synchrotron beam

In recent years, continuous development of synchrotron sources, such as 3rd generation synchrotrons and free electron lasers, has resulted in a dramatic increase in the coherence properties of beams especially in the hard X-ray region. The availability of such highly coherent and brilliant X-ray beams has triggered the development of new experimental methods based on coherence properties of synchrotron light and expanding the application area of existing techniques such as phase contrast imaging or X-ray holography [10, 61].

However unlike visible light sources, a beam produced by modern synchrotrons is not fully coherent. The characterization of the transverse coherence of X-rays at a sample position is important not only for planning and analyzing experiments but also for the development of instrumentation.

Here I put some techniques for measuring source size/transverse coherence to show that this isn't new problem and is has been developed for number of years. There are number of techniques for measuring of the transverse coherence or the source size have been performed recently [21, 58, 62-65]. Two general directions may be highlighted: measuring the source size and transverse coherence length.

The first and most obvious technique is direct imaging of the source and then – the measuring the size of the image. The image of the source is usually formed by a CRL [63], but also Fresnel zone plates [66] can be used but they are more complicated in operation and more suitable for soft X-rays due to low absorption of the material. It should be noted that the image formed by lens cannot be smaller than diffraction limit, so the imaging distance should be selected regarding to this fact. The principal experimental scheme is presented in figure 4.8.

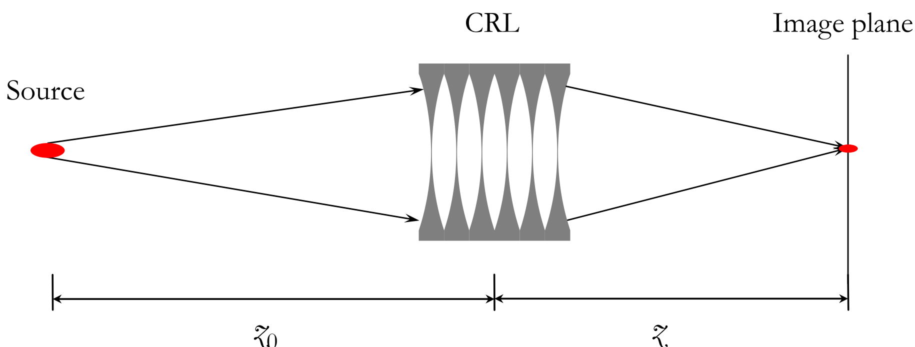

Figure 4.8. The imaging of the source experimental set-up.

Usually the observation distance z on the most of the beamlines is smaller than distance to the source z_0 and the geometrically demagnified source size denotes as:

$$S = \frac{z_0}{z} S' \tag{4.9}$$

where S' is the size of the image.

The transverse coherent length has been introduced earlier in equation (4.5), so the techniques sensitive to transverse coherence allow determination of source size by advertized equation. The technique of direct determination of transverse coherence was demonstrated in [58]. The transverse coherent length has been directly measured from the Fresnel diffraction pattern from Boron fiber. The principal experimental scheme is presented in figure 4.9.

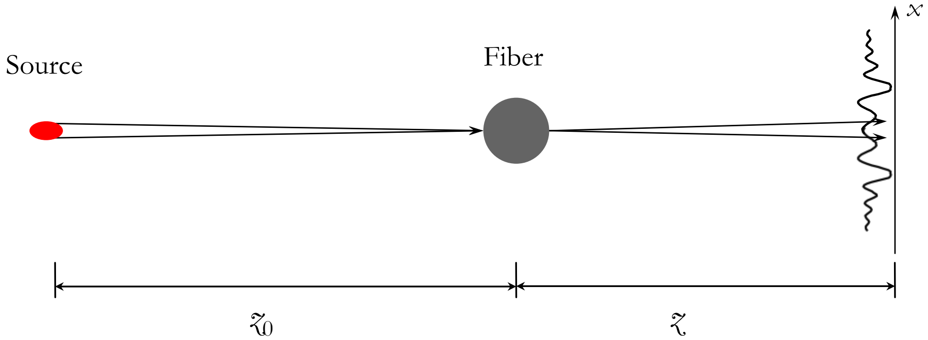

Figure 4.9. The fiber diffraction experimental set-up.

The registered image is the result of convolution of the source and the diffracted waves from point source on a fiber. The size of the source then may be calculated by the formula:

$$S = \frac{2\lambda(z_0 + z)}{\pi(|x| - R_{\mathrm{d}})} \ln^{1/2}\left(\frac{V_0}{V}\right) \tag{4.10}$$

where $|x|$ is the region of measuring the visibility (V) on the image, z_0 and z are distances from the source to the fiber and from fiber to the detector respectively, R_{d} is the projection of fiber radius on the image plane, V_0 is the visibility of the fringes in the case of point source. In addition to the

formula 4.10 authors also proposed another way to determine the source size from the fringe width [62]:

$$S \approx d_V z_0 / z \tag{4.11}$$

where the condition should be satisfied:

$$V d_V^{-3/2} \approx 0.08\delta (R_d / x)^{1/2} \lambda^{-3/2} \tag{4.12}$$

Another classical interferometric technique is Young double slit which I presented earlier. To determine the source size the theoretical fringe pattern (see eq. (4.6)) should be fitted to the experimental one by varying the source size as a parameter. Despite the fact that the result of measurement is the source size this technique is sensitive only to the transverse coherence, in other words to the correlation between waves propagated through slits (secondary sources). Others interferometric techniques are the variation of the Young technique.

5. The tunable double pinhole interferometer

5.1 Sensitivity to the source size fluctuation

Indeed, over the past 15 years, techniques based on or similar to the Young interferometer have become a typical way of source size measuring. The sensitivity of these techniques to fluctuations of the source size depends on the "aperture" of the interferometer i.e. the distance between slits. To demonstrate this I made the simulation of the interference pattern for number of different source sizes (from 36 µm to 46 µm with 2 µm step), and for slits separation of 40 µm and 120 µm. The illumination energy and distance to source were 12 keV and 50 m respectively. The spatial coherence lengths for 36 µm and 46 µm of source sizes are 140 µm and 110 µm respectively. The classical Young approach was used in calculations. A far field intensity distribution downstream of the interferometer can be expressed as [60]:

$$
\begin{gathered}
I(x) = I_0 \left[\sin(k_d x) \big/ k_d x \right]^2 \left[1 + V \cos(k_D x) \right] + I_b, \\
k_D = \frac{2\pi D}{\lambda z},\ k_d = \frac{2\pi d}{\lambda z}, V = \frac{\sin(\pi S D/\lambda z_0)}{(\pi S D/\lambda z_0)}
\end{gathered}
\tag{5.1}
$$

where D is the gap between apertures, S is the source size, d is the size of slit, z is an interference pattern observation distance, z_0 is a distance from the source to the interferometer, I_b is the background intensity.

To compare the sensitivity I used the fringe visibility parameter V. The fringe visibility modification with the slit separation for various sizes of the source is presented in figure 5.1.

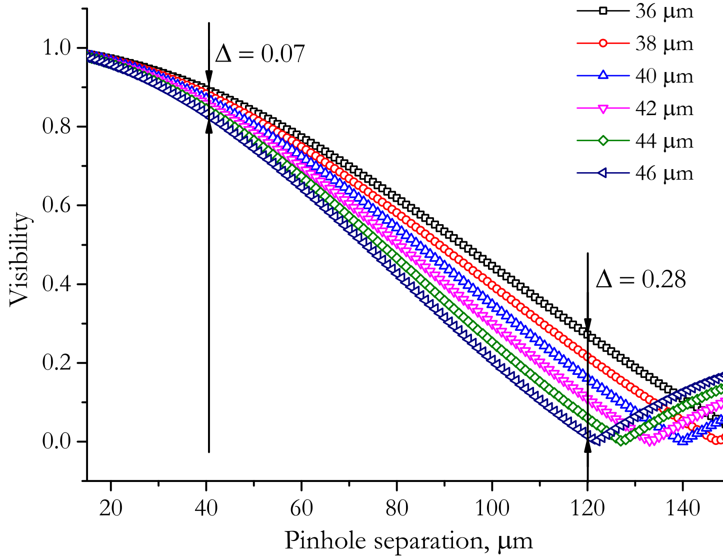

Figure 5.1. Interference fringe visibility modification with the pinhole separation for various sizes of the source. The colors represent different sizes of the source.

The absolute visibility modification Δ in the case of the 40 μm slit separation is only 0.07 while for 120 μm it is 0.28. Consequently to achieve high sensitivity to fluctuations of the source size the gap between slits should be as large as possible. On the other hand the size of the gap should not exceed the spatial coherence length, in order to obtain any interference visibility.

Currently the size of the source of 3rd generation synchrotrons approaching to several microns, for example, declared ESRF vertical source size is around 10 μm (It was discussed in chapter 2) and, usually, a sample position located approximately 50 m downstream. According to these parameters, in order to determine the source size, the gap between slits D should be (with 1 Å wavelength) about 600 μm (the size of the gap should be slightly greater than l_{coh} = 500 μm). To satisfy the far field criteria the observation distance should be much larger than $z = D^2/\lambda = 3600$ m. However the longest beamline at the ESRF allows to measure only 50 meters downstream of the sample and 100 m downstream from the source. On the other hand the effective source size is magnified by the factor of 3 or 4 due to the vibrations of monochromator and the reasonable gap between slits for the source size of 40 μm approaching to 100 μm that reduces the far field distance by factor 36 but it is still not enough to obtain far field pattern. In conclusion and in view of the geometrical limitations at synchrotron beamlines far field distance cannot be reduced.

Therefore there is the way to measure far field interference pattern at this distance: by using the refractive lenses, as I expressed earlier.

In fact, it is well known attribute of lenses, in case of a plane wave, at the back focal plane of lens the Fourier transform occurs (see equation 3.13) and this image may be considered as a far field image. The exact theory of the Fourier transform performed by lens and comparison with Fraunhofer diffraction pattern are presented in paragraph 3.3. This opportunity is widely applicable in the visible optics and particularly in the interferometry.

However unlike the visible light optics refractive lens for X-Rays has a minor difference. To perform Fourier transform in case of the visible light usually the detector is located at the back focal plane of the lens because a plane wave may be easily generated. Due to the short wavelength and finite distance to the source the lens focal distance may significant differs from the imaging distance and since the Fourier transform occurs in the imaging plane instead of focal plane this difference has to be taken into account whereas in the visible optics it may be neglected.

The experimental interference fringe visibility can be affected by a number of natural factors (CCD noise, statistical errors, etc.) which adversely affect the precision of the source size determination. To increase the reliability of the results a series of measurements with different gaps between slits have to be done. This allows to register the dependence of the visibility modification as a function of the slits separation in order to raise the precision of the source size determination. In this chapter I will describe the tunable double slit interferometer with the high sensitivity to the source size fluctuations.

5.2 The concept of the interferometer

To manufacture the tunable double slit system high quality disk apertures for use in an electron microscope were chosen. These apertures were manufactured to tight tolerances with precision drilled holes. The discs were made from a platinum/iridium alloy 95.5% and the apertures are made with a hole size of 11 μm. The diameter of the substrate was 2 mm. The minimum thickness of the aperture is above 25 μm whereby the attenuation of X-rays below 19.3 keV (absorption edge) is above 99%. Therefore the transparency of the material can be neglected.

Using the Leica EM TXP target surfacing system substrates were cut from the side at ~ 80 - 90 μm distances from the centre of the hole. The scanning electron microscope image of cutout aperture is shown in figure 5.2.

The apertures were located at separate translation stages allowing alignment in the beam. To provide all the range of separations apertures were arranged with overlapping of cut parts (see Figure 5.3 (a)), one downstream relative to another at the distance ~ 2 mm. Therefore, this distance may be neglected and assumes that apertures are located in the same position relative to the source. To avoid the primary beam passing between holes the maximum separation was reduced by 10 μm so that the split distances between holes varied in the range 90 - 160 μm. As the source is much smaller vertically, the apertures were oriented so as the top aperture moved relative to the bottom one in the vertical direction.

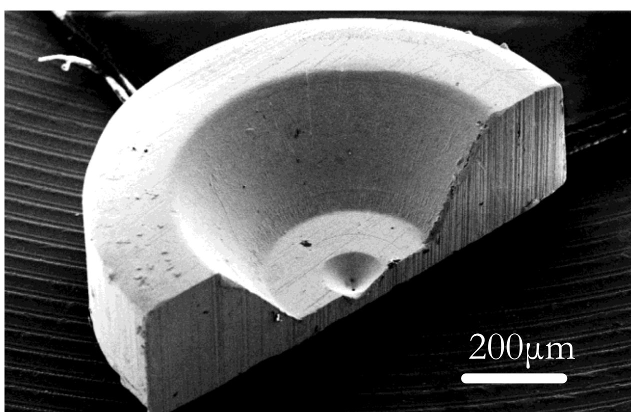

Figure 5.2. SEM image of cutout platinum pinhole.

Moreover there is another, more complicated way to collocate pinholes in the beam to achieve wider range of split distances. One pinhole should be moved relative to another along the cut edge, at the same time to remain vertical displacement of holes all system of 2 pinholes should be rotated in the necessary direction around the imaginary centre between holes as shown in the Figure 5.3 (b). In the experimental tests only first arrangement was used because it covers all range of experimental parameters and less sophisticated in use.

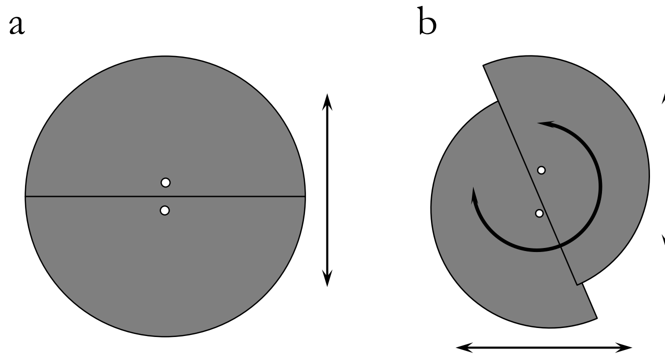

Figure 5.3. Two types of arrangements of pinholes in a beam.

5.3 Experiment

The experimental tests of tunable double apertures were carried out at the MOTB at the ID 06 ESRF beamline. To reduce the influence of the third undulator harmonic, the second crystal of the monochromator was slightly detuned from the Bragg position. The detuning angle was around 10 µrad (2 arc. sec.) to provide the remaining fundamental harmonic flux of about 80%. A sketch of the principal experimental scheme is presented in Figure 5.4. The typical exposure time varied between 20 s and 60 s depending on the aperture separation and the current of the storage ring during a 7/8 beam bunch mode (~200 mA current). To verify the measurements by the Young double slit apparatus the source size was measured using imaging by refractive lenses [63], and determining that the vertical source size of 39 µm was in full agreement with previous tests on this beamline.

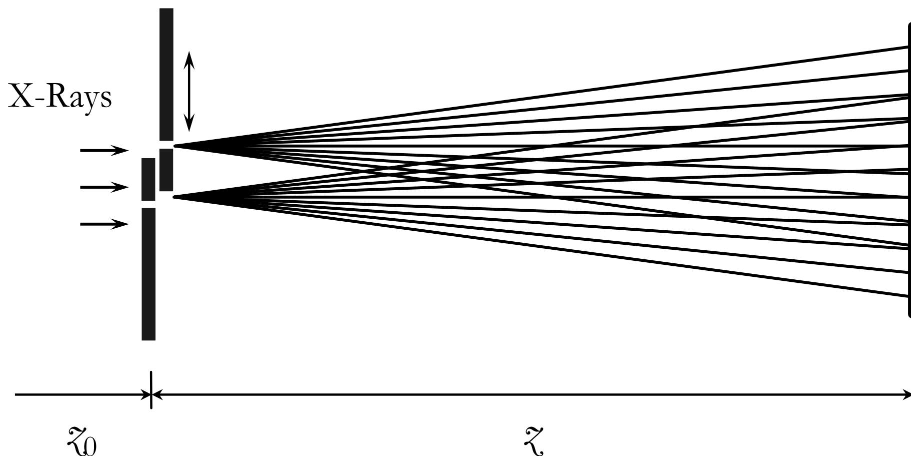

Figure 5.4. The experimental scheme sketch of the Young interferometer setup.

Interference patterns with different aperture separation without refractive lenses have been registered to visually confirm the necessity of refractive lenses utilization. The illumination energy was 11 keV, the observation distance z = 15.2 m from the interferometer. Figure 5.5 presents the recorded interference pattern rotated by 90 degrees and an intensity variation obtained for the line through the centre of the pattern.

The period of the interference pattern is 18 µm that is in agreement with theoretical calculations. At the same time the fringe visibility of 0.4 is less than theoretical of 0.54 for the source of 40 µm measured previously.

The mismatching of the visibility is caused by partial overlapping of cones from pinholes, in other words, the far field condition is not satisfied.

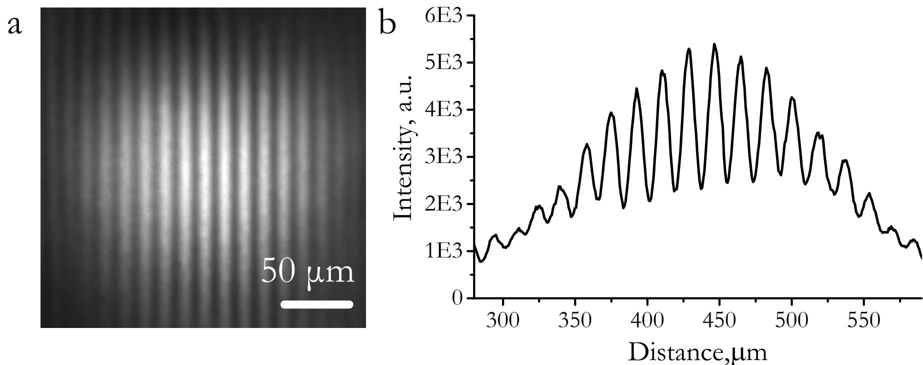

Figure 5.5. The 90 degree rotated registered interference pattern for 90 μm separation of pinholes – (a) and its cross section (orthogonal to fringes) – (b).

To raise the visibility as I expressed above the refractive lenses should be used. The experimental scheme sketch is presented in figure 5.6. The experiment was carried out with 9.2 keV illumination energy (1.35 Å wavelength), 6 Be refractive parabolic lenses with the curvature radius of 200 μm and the focal distance of $F = 4.15$ m. were located at the distance $z_1 = 20$ cm from the interferometer, the CCD camera was placed at the distance $z = 4.4$ meters from the lenses (imaging distance of the source), because the distance to the source z_0 is finite the imaging distance for the source z differs from the focal distance. The effective aperture of CRL was about 900 μm and it is significantly large than the maximum gap between apertures of 130 μm that made it possible exclude from consideration the size of the lens and assume it was infinite.

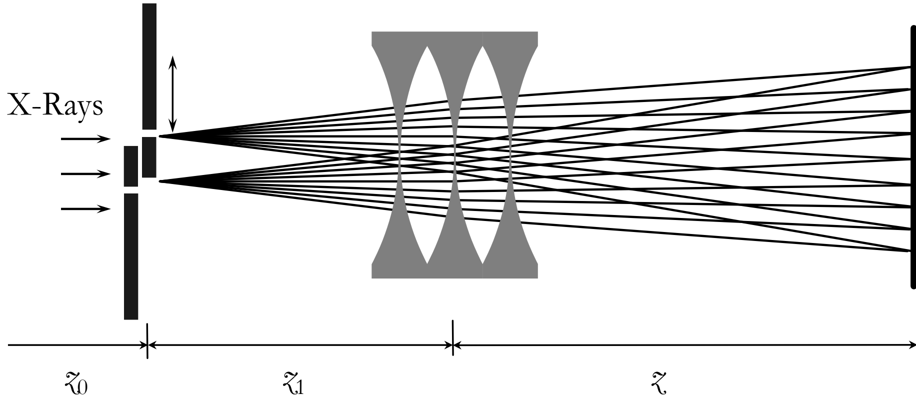

Figure 5.6. The experimental scheme sketch of the Young interferometer setup with the use of CRL.

The interference pattern without lenses was recorded in the near field (4.6 meters observation distance). Figure 5.7 presents the interference pattern (a) and the cross section (b) for 90 μm pinhole separation. It is clear to see that the observation distance is not enough to obtain any reasonable visibility as diffracted beams are not overlapped and the interference visibility is about 0.05 (while the theoretical for 40 μm source is about 0.55).

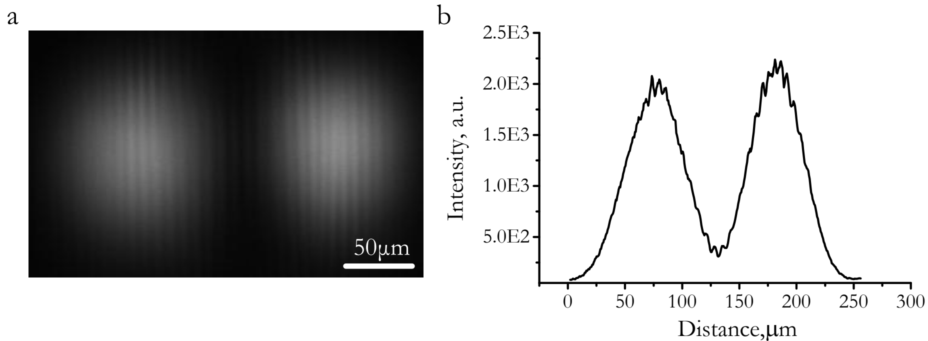

Figure 5.7 The 90 degree rotated interference pattern for 90 μm separation of pinholes recorded without CRL – (a) and its cross section (orthogonal to fringes) – (b).

Upon inserting the lens the fringe visibility is proved as in the far field (see paragraph 3.3). The interference pattern recorded on the observation distance 4.4 meters downstream of the lenses and its cross section are presented in figure 5.8 (a) and (b) respectively. The period of the interference pattern is 6.5 μm that is in agreement with theoretical calculations by the equation (5.1).

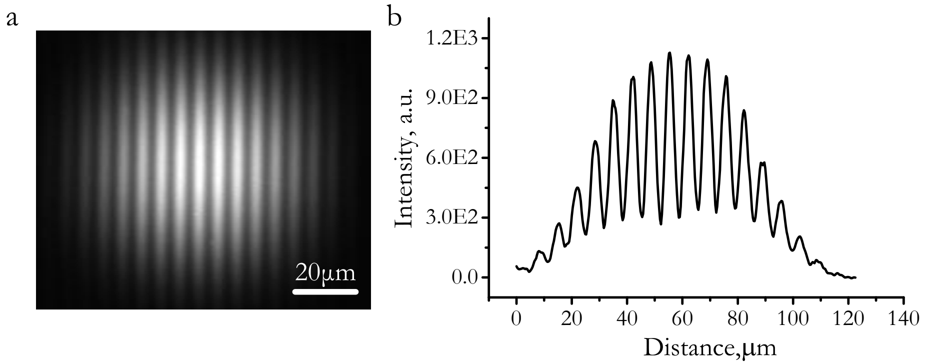

Figure 5.8 The 90 degree rotated interference pattern for 90 μm separation of pinholes recorded with CRL – (a) and its cross section (orthogonal to fringes) – (b).

The situation has been changed by the refractive lens utilization: the interference fringe visibility raised to 0.56 that is corresponds to the approximate size of the source about 40 μm. Finally the modification of the fringe visibility with different pinhole separation was recorded.

To precisely determine the source size, the numerical evaluation was carried out either by fitting the fringe visibility modification calculated from the theoretical intensity by the equation (5.1) to the experimental one for different aperture separation. Experimentally determined values of the fringe visibility (dots) for different aperture separation together with theoretical calculation (line) for the source size of 39.7 ± 1.3 μm (best fit, $\chi^2 = 0.2$) are presented in figure 5.9 The value is in full agreement with the result of the measurement of the source using refractive lenses earlier.

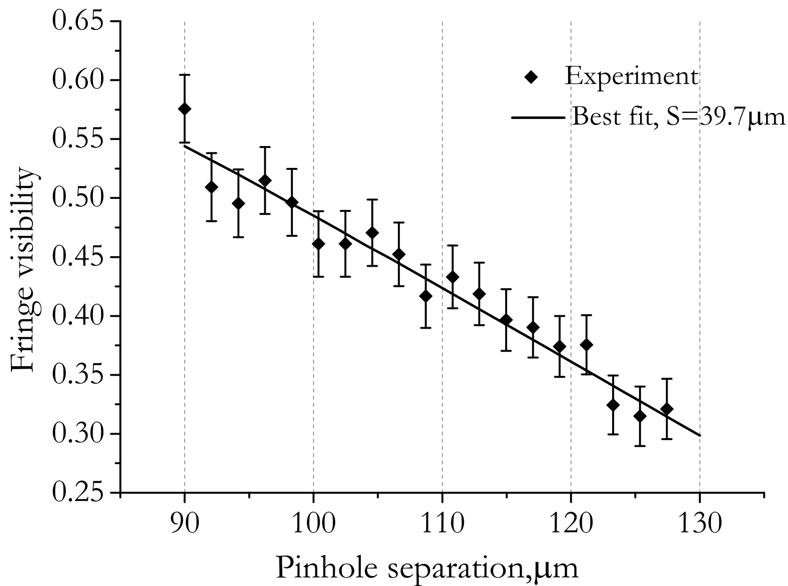

Figure 5.9 The experimental fringe visibility (dots) and the theoretical calculation - best fit (solid) for 39.7 μm size of the source.

5.4 Discussion

The technique for the source size measurements is proposed and tested at the beamline ID 06. The effective source size has been measured, the value is in full agreement with the result of the measurement by other technique. The variable distance between holes got raises the sensitivity of measurements to the modification of the source size from microns to millimeters depending on the holes displacement. The use of refractive lenses allowed to get rid from the partial overlapping of diffracted beams which in turn expand the applicability of this technique.

It should be noted that with the use of refractive lens the interference pattern observation distance has been reduced from z = 15 m. (not complete far field) to the z = 4.6 m., therefore the setup with lens is much more compact and as the result can be used more widely on beamlines with limited space.

The approach for the measurements of the source size demonstrated in this chapter allows to improve the understanding of the limitations of the interferometric techniques for the study of the transversal coherence.

6. Multilens interferometers

It has been discussed earlier (in chapter 2) that refractive lenses have very wide field of applications and directions of development (such beam conditioning, Fourier optics and coherent diffraction imaging). In this chapter I will discuss another promising direction of refractive optics development - in-line X-ray interferometry. For example, recently proposed bilens interferometer [24], which I described in chapter 4, under coherent illumination formed two secondary sources, then at some distance beams from these sources overlap resulting in an interference field with variable period depending on observation distance. Analogous to Young's interferometer it generated interference field that laterally nonlocalized, it exists everywhere in the region of overlap. As an evolution of this system a multilens interferometer in which more than two parallel lens arrays are arranged was designed and manufactured. The enlargement of the interferometers acceptance gives rise to increased contrast of the interference pattern, and a narrowing of the interference fringes.

6.1 The concept of multilens interferometer

While the bilens interferometer produces a steadily expanding sinusoidal interference field, the multilens arrangement substantially changes the interference pattern by adding a strong longitudinal functional dependence which can be described by Talbot imaging formalism.

I emphasize that in the case of a multilens interferometer, the classical grid used for Talbot imaging is replaced by a collection of periodic line secondary sources produced by linear lens arrays separated by the distance *d*. It is should be noted that the Talbot distance is measured from lens foci and that these foci are reproduced in both the Talbot planes and fractional Talbot planes.

It was manufactured two sets of multilens interferometers, consisted 6 (hexalens) and 30 (triacanta) lens in one chip upright. The SEM images of these interferometers are presented in figure 6.1

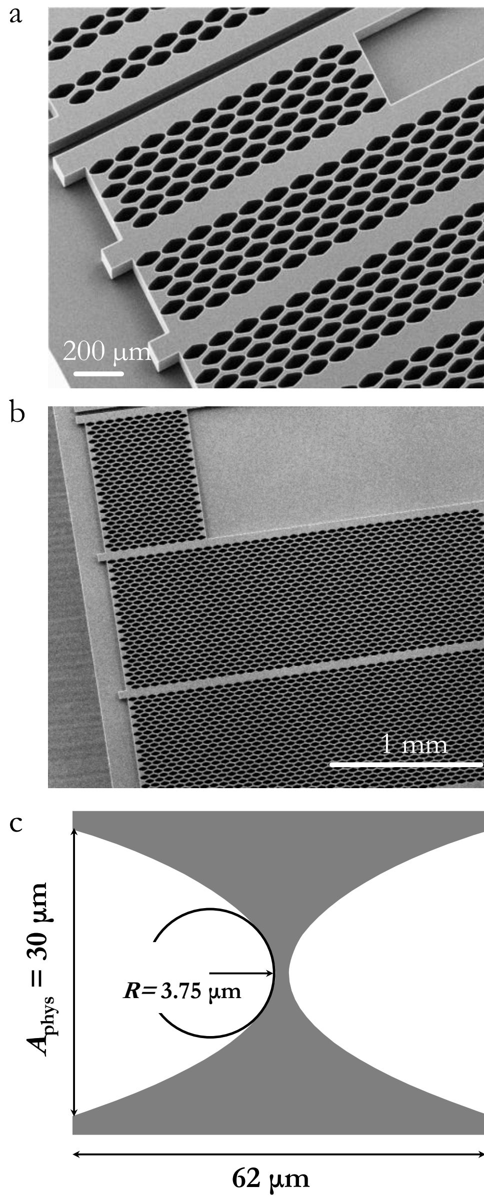

Figure 6.1 SEM images of multilens interferometers: 6 lens interferometer – (a) and 30 lens interferometer – (b). A schematic view of a single lens – (c).

It consists of six or thirty arrays of identical, parallel planar compound refractive lenses (CRL) separated transversally by a distance d. Each compound refractive lens focuses the beam at the distance $z_F = F/(1-F/z_0)$, where $F = R/2N\delta$ is the lens focal length and z_0 is the source-to-lens

distance, R is the radius of curvature of one parabolic surface, N is the number of double concave elements in the CRL, δ is the decrement of complex refraction index $n = 1-\delta+i\beta$. Under coherent illumination each lens generates a coherent, diffraction limited focal spot of size $w_f = 0.44\lambda z_f/A_{eff}$, where λ is the wavelength and $A_{eff} = 0.66(\lambda z_f\delta/\beta)^{1/2}$ is the absorption limited effective aperture of the lens [18]. The beams from secondary source will have a finite divergence and overlap each other in the central part of interference pattern at the distance larger than $z = z_f A_i / A_{eff}$, where A_i is the interferometer aperture.

The interferometers were manufactured using a process involving electron beam lithography and deep etching into silicon which I described in previous chapter. The length and aperture of each double concave individual lens are 62 μm and 30 μm respectively (see figure 6.1 (c)). Structures are 70 μm deep. The radius of the parabola apex is R = 3.75 μm and the minimum thickness between the parabola apexes is 2 μm. The split distance between lens arrays in the interferometer is d = 30 μm.

With the aim to simplify the use of interferometers in the experiments where energy tunability is required, five sets of the interferometers were manufactured on the same Si chip. All interferometer sets have a fixed focal distance (F = 4 cm) for the chosen energy that was achieved by varying the numbers of individual lenses in each lens array. The chip covers a considerable X-ray energy range from 10 to 50 keV. To choose the desirable working energy, one can switch from one interferometer set to another by a parallel displacement of the chip in the vertical direction. The main parameters of the interferometer sets are summarized in the table presented below.

Set number	Energy, keV	Number of lenses	Lens length, μm	Diffraction Limited Resolution, nm	Effective aperture, μm
1	10	10	618	190	13
2	20	39	2416	87	17
3	30	87	5392	63	21
4	40	156	9670	55	23
5	50	243	15064	53	23

Table 6.1 Parameters of multilens interferometers.

6.2 Theory

Here I will provide the theoretical estimations which describe the multilens interferometer. These estimations have been made by V. Kohn [67].

The wave field of radiation from the point source at the distance z_0 is described by $\exp(ikz)P(x,z)$, where

$$P(x,z) = \frac{1}{(i\lambda z)^{1/2}} \exp(i\pi \frac{x^2}{\lambda z}) \quad (6.1)$$

is the Fresnel propagator which is a part of spherical wave in the paraxial approximation. Here λ is the wavelength, x is a transverse coordinate and z is the coordinate along the optical axis. The exponential term $\exp(ikz)$ can be omitted because it does not influence the intensity. Let's consider the multilens interferometer, which consists of M arrays of CRLs separated by distance d. The length of the interferometer is much smaller than the distance to the source. Therefore, to study its optical properties the interferometer can be treated as a phase object which can be taken into account by the transmission function:

$$T(x) = \exp(-ik\,[\delta - i\beta]t(x)) \quad (6.2)$$

where $t(x)$ is a variable thickness of the M-lens interferometer along the ray parallel to the optical axis. Here $t(x)$ is the sum of the thickness of each CRL:

$$t_{\mathrm{m}}(x) = N(x - x_{\mathrm{m}})^2 / R, x_{\mathrm{m}} = d(m - \frac{M+1}{2}), m = 1, \ldots M \quad (6.3)$$

where N is a number of individual lenses in the CRL, R is a curvature radius, x_m is a position of the m-th lens center, and M is a number of CRLs in the interferometer. The gap between CRL is equal to zero and the aperture of each lens is d, then the condition $|x - x_{\mathrm{m}}| < d/2$ has to be taken into account in equation 6.3.

A propagation of the wave through free space on the distance z_1 between the interferometer and the detector is described by a convolution of the wave function and $P(x, z_1)$. The total expression can be transformed to a new form as a product $P(x, z_T)$ and a convolution of $T(x)$ and $P(x, z_r)$, where

$z_T = z_0 + z_1, z_r = z_0 z_1 / z_T$. From this, a relative intensity is calculated as follows:

$$I(x) = |a(x_0)|^2, a(x_0) = \int dx_1 P(x_0 - x_1, z_r) T(x_1), x_0 = x z_0 / z_T \qquad (6.4)$$

It should be noted that if z_0 is not large compared to z_1 then the image is magnified compared to the object, however, all features of the image stay the same. The finite size of the source may be taken into account by a calculation of the convolution of the intensity for a point source and Gaussian with FWHM as $S(z_1+z_F/z_0)$ where S is the source size.

Nevertheless, the properties of multilens interferometer can be formulated without calculations described above. It is clear that the M-lens interferometer transforms the incoming parallel beam to M sets of divergent beams behind the focusing distance z_F. These focal lines are placed periodically in space along the axis x with the period d.

The secondary sources coordinates denotes as $x_m = d(m - (M+1)/2)$, $m = 1,\ldots M$. Then the ray paths are:

$$r_m = (z^2 + x_m^2)^{1/2} \approx z + \frac{x_m^2}{2z} = z + \frac{d^2}{z} \frac{(m-(M+1)/2)^2}{2} \qquad (6.5)$$

The goal is to determine the distances z where rays from all sources come to the optical axis ($x = 0$) with the same phase or with a difference which is integer number of 2π. It is clear that the relative intensity will be increased from 1 to M^2 at such distances. One can calculate the ray path r_m from m-th CRL to the optical axis at the distance z from the sources and consider a difference of ray paths for the arbitrary m and j sources. The result is:

$$r_m - r_j = r_{mj}^{(0)} = \frac{d^2}{z} \left[(m-j) \left(\frac{m+j}{2} - \frac{M+1}{2} \right) \right] \qquad (6.6)$$

Since m, j, M are integer and M is even the expression in the square brackets is also integer. Indeed, if $(m - j)$ is odd then $(m + j)$ is odd too and the expression in the second round bracket is integer. If $(m - j)$ is even then the expression in the round bracket is semi-integer but it is multiplied by even integer.

Thus the condition for constructive interference of the secondary sources produced by M CRLs of the interferometer can be written as $d^2/z =$

λn where n is arbitrary integer number. Distance $z_T = 2d^2/\lambda$ is a fundamental Talbot distance where the set of M periodic line sources are reproduced. Halfway to the picture, a secondary fundamental Talbot image is formed (it is shifted vertically from the primary image by the half of a period). At distances $z_n = d^2/(\lambda n) = z_T/2n$ between primary and secondary Talbot images the infinite family of fractional Talbot images can be observed.

If the source is located at the distance z_0 from the interferometer and this distance is comparable with observation distance the fractional Talbot images will be magnified by the factor $C_m = (z_F + z_n' + z_0)/(z_0 + z_F)$ and will be located at the distance z_n' which is obtained from the equation:

$$\frac{1}{z_F + z_n'} + \frac{1}{z_0} = \frac{1}{F + z_n} \tag{6.7}$$

The next step is to calculate the period of the interference fringes.

$$r_m - r_j = r_{mj}^{(0)} - \frac{xd}{z_n}(m-j) = r_{mj}^{(0)} - \lambda n \frac{x}{d}(m-j) \tag{6.8}$$

This expression shows that the period of interference fringes is $\Lambda = d/n$. The case where $M = 2$ is special because the expression in the square brackets of equation (6.6) is equal to zero, therefore the high contrast, sharp interference pattern exist at any distance. Correspondingly, the period depends directly on the distance and is equal to $\Lambda = \lambda z/d$.

The width w_t of the interference fringe maximum across the beam will be estimated below.

I will assume that the distance z is sufficiently large and all beams from CRLs can interfere. In this case each secondary source can be replaced by the point source which is described by the function $P(x, z)$. Then, intensity can be written as $I(x,z) = (\lambda z)^{-1} K_F(x,z)$. Initially the function $K_F(x,z)$ is a sum of M and a double sum of cosines of complex argument which contains the coordinates of all CRLs. The double sum can be reordered to a more suitable expression which can be simplified significantly in the case of $z = z_n, j = m - q$, $q = 1,2,3...m - 1$.

$$K_F(x, z_n) = M + 2\sum_{q=1}^{M-1}(M-q)\cos\left(2\pi\frac{q}{\Lambda}x\right), \quad \Lambda = \frac{d}{n} \tag{6.9}$$

It should be noted that this expression is valid for the finite M secondary sources produced by the interferometer, while the Talbot effect is applicable for the infinite periodic system. The period of the fringes does not depend on M; whereas the fringe intensity of the interference pattern is determined by M. For $x = 0$ we have $K_F(0,z_n) = M^2$, at the same time a mean value of the fringe intensity averaged over the fringe period is equal to M.

To estimate a fringe width it should be noted that a numerical calculation of $K_F(x,z_n)$ shows that for large M it is a fringe which can be described approximately by a Gaussian: $K_F(x,z_n) \approx M^2\exp(-\alpha x^2)$. The parameter α may be calculated from the first term of the expansion (7.9) in power series. As a result:

$$\alpha = \left(\frac{2\pi}{\Lambda}\right)^2 \frac{M^2-1}{12}, \quad w_t = \frac{1.7}{\alpha^{1/2}} = \Lambda \frac{0.92}{(M^2-1)^{1/2}} \tag{6.10}$$

The longitudinal fringe size may be calculated similarly from (7.9):

$$w_l = \frac{7.1\Lambda^2}{\lambda M^2} \approx 8.44\frac{w_t^2}{\lambda} \tag{6.11}$$

The relations expressed above are obtained for the fully coherent irradiation, if it is not the case, the angular source size S/z_0 has to be taken into account. In this case l_{coh} has to be more than A_i. If not, then only part of the CRLs can interfere which number is equal to $M_e = l_{\text{coh}}/d$.

Because on the Talbot image is secondary diffraction limited sources reproduction. The source size S can be directly estimated from the width of the interference fringe (for the fundamental Talbot image) is based on the source size projection to the detector which is estimated as $S' = SC_s$, where $C_s = (z_F + z_n')/z_0$. If this size is much more than the diffraction limited width of the interference fringes $w_t' = w_t C_m$, then the FWHM w_e of the experimental fringes allows one to estimate the source size directly as $S = w_e/C_s$. In more complicated cases the convolution of the source size projection and the computer simulations of the diffraction limited width of fringes have to be done.

6.3 Multilens interferometers optical properties study

6.3.1 Sixlens interferometer

The experimental tests of the sixlens interferometer were carried out at the MOTB of the ID06 ESRF beamline. The sketch of the beamline and range of possible experimental parameters were presented in chapter 2. The Si sixlens system was mounted at the stage with all necessary rotation and translation movements at a distance z_0 = 54 m from the source. The principal experimental scheme sketch is presented in figure 6.2.

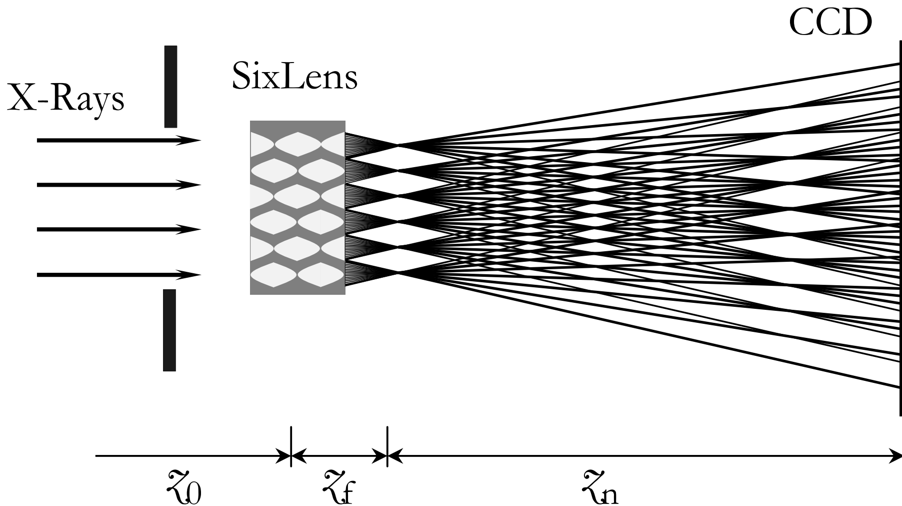

Figure 6.2. The experimental scheme sketch of the six lens interferometer setup.

Interference patterns were recorded with a high resolution X-ray CCD camera ("Sensicam") with a spatial resolution about 1.3 μm (0.65 μm pixel size). The typical exposure time was 2 seconds during a 7/8 beam bunch mode (200 mA current).

As it was mentioned earlier, the foci of the six lens arrays in the interferometer form a periodic structure and therefore the foci are reproduced at the Talbot distances with a different scale depending on the fraction of Talbot distance. Considering the parameters of hexalens it can be easily estimated that for 12 keV X-rays, the Talbot distance z_T is in the order of 18 m (in the case of plane wave). Taking into account the beamline characteristics (energy range, length) and CCD spatial resolution, the interference fringes were observed at the fractional Talbot distances z_n.

Therefore the CCD was always placed at distance $z = z_F + z_n$. The quality of the fringes produced by a multilens system can be described quantitatively using the visibility parameter.

To characterize the interferometer at 12 keV, the fractional $n = 3$ Talbot distance which corresponds to $z_n = 3$ m was chosen. The observed interference pattern and the comparison of theoretical and experimental intensity variation obtained for the line through the center of the fringe pattern are shown in figure 6.3. The measured fringe spacing was $\Lambda = 10.3$ µm, which is in very good agreement with the calculations. The measured FWHM of the fringe maximum is 3 µm, while according to the calculations it should be around of 1.7 µm. The broadening of the measured fringe width is caused by the finite size of the source. The source size was measured by a B-fiber interferometry technique [58], which during the interferometer tests was in the order of 45 µm. The measured fringe visibility was approximates 0.73, while the theoretical one was around 0.88. For the 45 µm source size at 54 m from the source the spatial coherence length is in the order of 130 µm. While the width of the interferometer is 180 µm, thus the partially coherent illumination reduces the contrast of the fringe pattern.

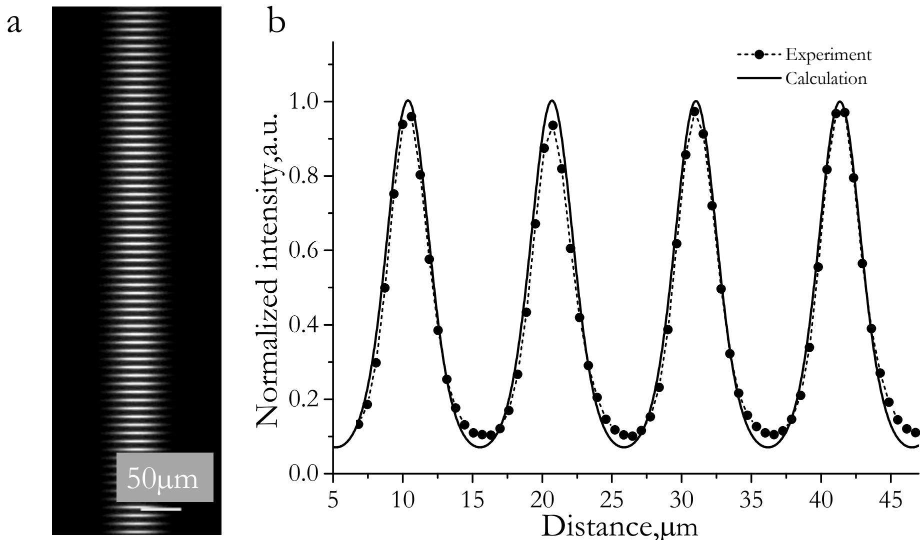

Figure 6.3. An interference pattern generated by a hexalens, recorded with 12 keV X-rays – (a). The comparison of the intensity variations of the interference pattern experimentally measured and calculated one – (b).

Let me estimate the stability of the interference pattern in terms of depth of field. Similar to the criteria for refractive lenses depth of focus [44], I

define the interferometer depth of field as a range of distances along the optical axis trough which the lateral size of interference fringe (FWHM) is less than √2 of its value at the exact Talbot imaging distance. For this I placed the hexalens at the distance z_n = 3.06 m and then scanned it along the optical axis in the interval ± 100 mm with 1 mm step around exact position. At each position the interference pattern was registered and the lateral size of the interference fringe was measured together with the contrast. Regarding the criteria expressed above a depth of field in the order of 80 mm was obtained which is in a very good agreement with the value calculated by equation (6.11). For the CRL focal spot of the same size the value of the depth of field is 16 mm. It should be noted that within these depth of field the fringe contrast was reduced in the order of 0.2. For practical applicability of the interferometer the large depth of field is very important.

The sixlens interferometer was tested with 24 keV X-rays and the interference pattern was registered at the fractional n = 6 Talbot distance which is z_n = 3 m. Experimentally measured fringe spacing of the recorded interference pattern was 6.3 μm and FWHM of the fringe maximum was 2.7 μm. The measured contrast was around 0.4, which is 0.3 lower than was expected from the calculations for the point source. It should be noted that the spatial coherence length at 24 keV is in the order of 70 μm. This means that only 3 lens arrays are illuminated coherently, which leads to the broadening of the interference fringes and decreasing of the fringe visibility.

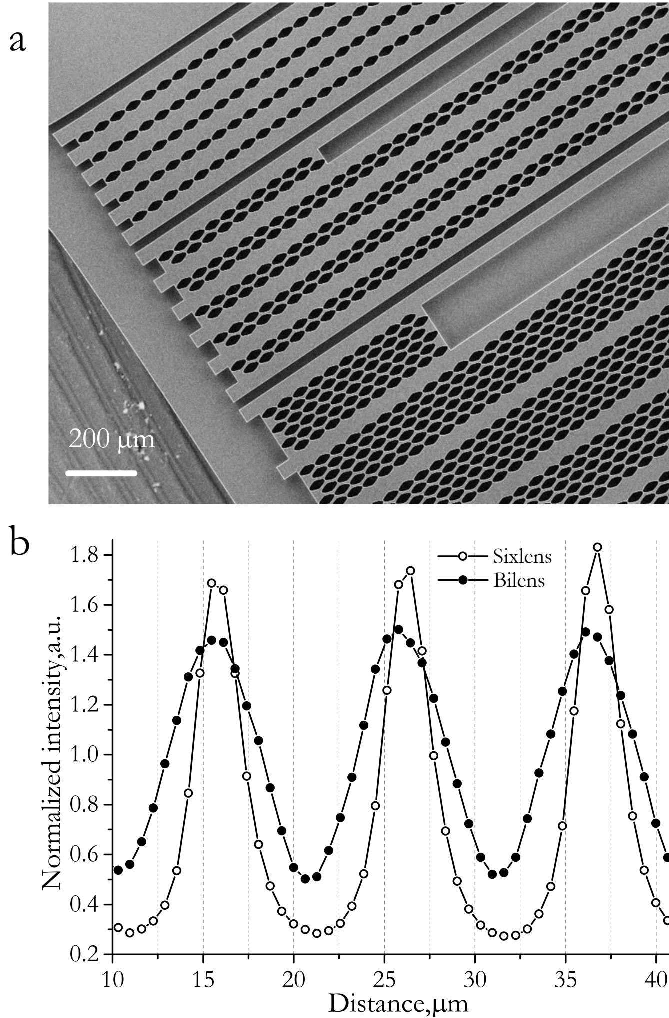

Figure 6.4. SEM image of chip consisted of bilens and sixlens interferometers – (a), comparison of interference patterns generated by sixlens and bilens interferometers – (b).

To demonstrate the narrowing of the interference fringe maximum in the case of the hexalens, the interference pattern produced by a bilens interferometer (located in the same chip, see figure 6.4 (a)) was recorded under identical experimental conditions: X-ray energy was 12 keV and distance z_n = 3.06 m. The bilens interferometer consists of two lens arrays with the separation period of 30 μm. The measured fringe spacing of the bilens interference pattern was Λ = 10.3 μm.

The comparison of the intensity variation through the center of the fringe pattern for the bilens and sixlens interferometers is shown in figure 6.4 (b). The measured FWHM of fringe maxima for the bilens

interferometer is 5.2 μm, as for the sixlens interferometer it is 3 μm. The results show a narrowing of the interference fringes but not as much as expected. As discussed above, the reason for this is a finite source size and partial coherent illumination. It is clearly seen that the contrast of the fringes produced by sixlens interferometer is superior to the fringe contrast of the bilens.

Hexalens was also experimentally tested with the point secondary source produced by Si planar refractive lens. The sketch of the experimental setup is shown in figure 6.5.

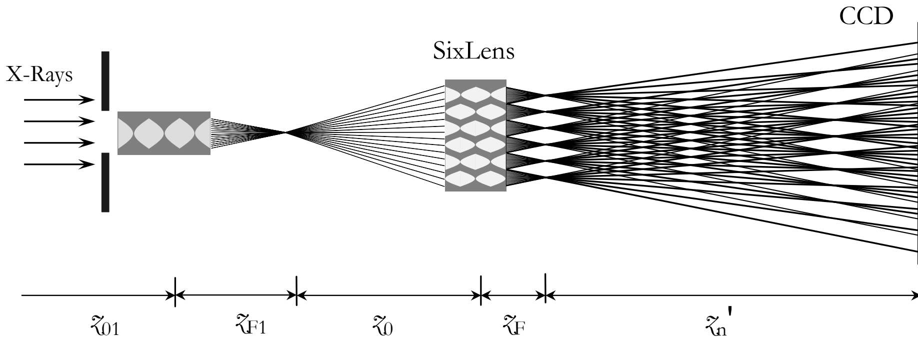

Figure 6.5. The experimental scheme sketch of the setup with secondary source.

The lens consisted of 26 individual lenses with radius of parabola apex of 6.25 μm and aperture of 50 μm. The Si lens was located at z_{01} = 55 m from the source. At energy E = 12 keV it has a focal distance z_{F1} = 3.5 cm. The interferometer was placed at the distance z_0 = 550 mm from the secondary source. In the case where incident radiation comes from a point source at a finite distance z_0, the spherical wave approximation has to be considered. It is readily shown that the fractional Talbot image will be magnified by a factor $(z_n + z_0 + z_F)/z_0$ and interference occurs at the distance z_n' given by equation (7.6):

$$\frac{1}{z_F'+z_n'}+\frac{1}{z_0}=\frac{1}{z_F+z_n},\ z_F=\frac{R}{2\delta N},\ z_n=\frac{d^2}{\lambda n},\ z_F'=\frac{z_F}{1-z_F/z_0} \qquad (6.12)$$

A high order fractional n = 20 Talbot image was registered at the distance z_{20} = 3.8 m from the lens array foci, with a magnification factor of around 7. The measured fringe spacing is 11.5 μm and FWHM of the interference fringe maximum is 3.1 μm. The measured visibility of the interference pattern is 0.915, which corresponds to the secondary source size in the order of 220 nm. It should be mentioned that for the plane wave illumination, the n = 20 fractional Talbot image can be registered at 45 cm distance from the lens focal lines. The period of the fringe pattern is

1.5 μm and the FWHM of the fringe maximum is 0.25 μm which beyond the resolution of current CCD with scintillation screen based X-Ray detectors.

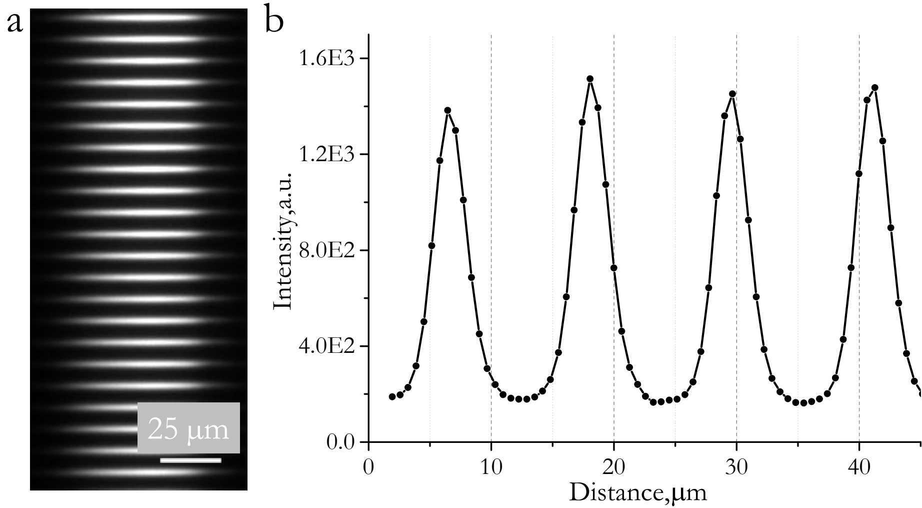

Figure 6.6. An interference pattern generated by a hexalens illuminated by point secondary source with 12 keV X-rays – (a). The intensity variation of the experimentally measured interference pattern – (b).

6.3.2 Thirty lens interferometer

The experimental tests of the 30 lens interferometer were performed at the long (about 100 m) ID11 ESRF beamline. The experimental scheme sketch is shown in Figure 6.7 (a). The source size S was measured using CRL imaging [63] which during the 30 lens interferometer tests was in order of 15 μm.

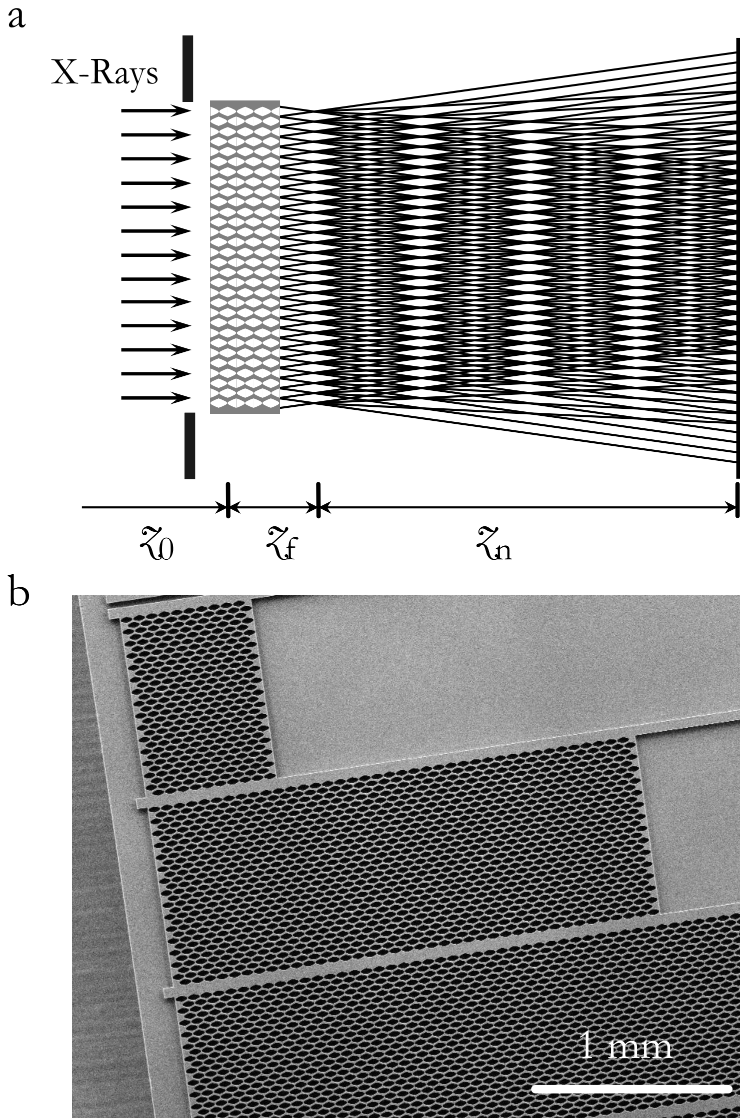

Figure 6.7. The experimental scheme sketch of the thirty lens interferometer setup – (a), SEM image of chip consisted of thirty lens interferometers – (b).

The triacanta was mounted on the stage with all necessary rotation and translation movements allowing alignment in a beam at the distance z_0 = 41.4 m from the source. At this distance, under 32 keV illumination, the spatial coherence length (according to the estimated source size of 15 μm) l_{coh} = 110 μm, hence only 4 nearest CRLs was under coherent illumination.

The registration of the interference patterns was performed by the high resolution X-ray CCD camera ("FReLoN") equipped with a fluorescence screen and an optical objective allowed to obtain 3 μm of spatial resolution (1.5 μm pixel size).

The typical exposure time was 20 – 60 seconds depending on the irradiation energy during a 7/8 beam bunch mode (200 mA current).

Taking into account the beamline characteristics such as an energy range, available distances, and an efficiency of the CCD camera in order to characterize the interferometer optical properties with 32 keV irradiation energy, the fundamental $n = 1$ Talbot image which corresponds to the distance $z_1' = 53$ m was chosen. This image has a period as the object period for the parallel beam but with fringes location shifted on the half period.

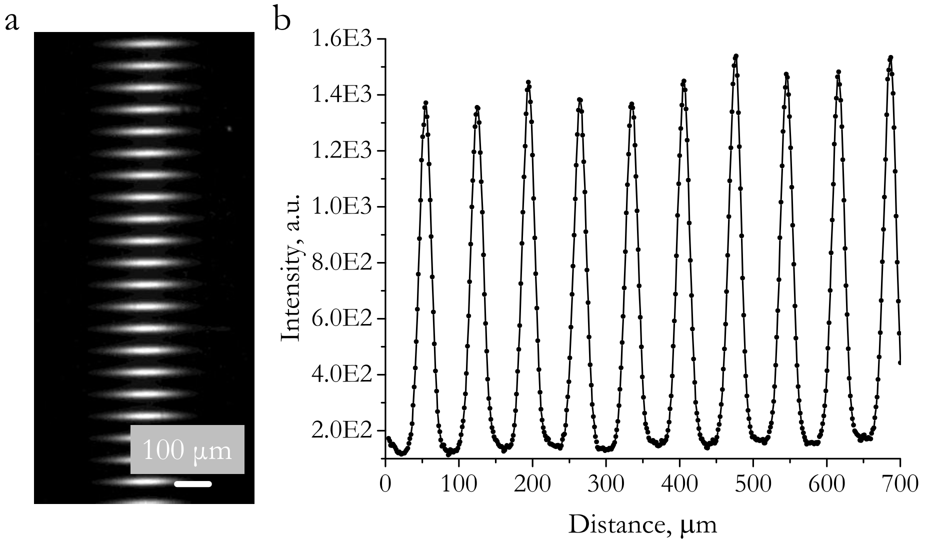

Figure 6.8. An interference pattern generated by Triacanta recorded with 32 keV – (a). The intensity variation obtained for the line though the centre of the fringe pattern, the contrast visibility is approximately 0.86 – (b).

The registered interference pattern and the intensity variation obtained for the line through the centre of the pattern orthogonal to fringes are shown in figure 6.8. The registered fringe spacing is $\Lambda = 68$ μm which corresponds to the theoretical estimation. The interference fringe visibility is 0.86. The measured interference fringe FWHM is 20 μm and it is possible to assume that it is equal to S'. Then the estimation of the source size is obtained as $S = S'z_0/z_1' = 15.6$ μm that is in a good agreement with the result obtained by means of CRL imaging of the source - 15 μm.

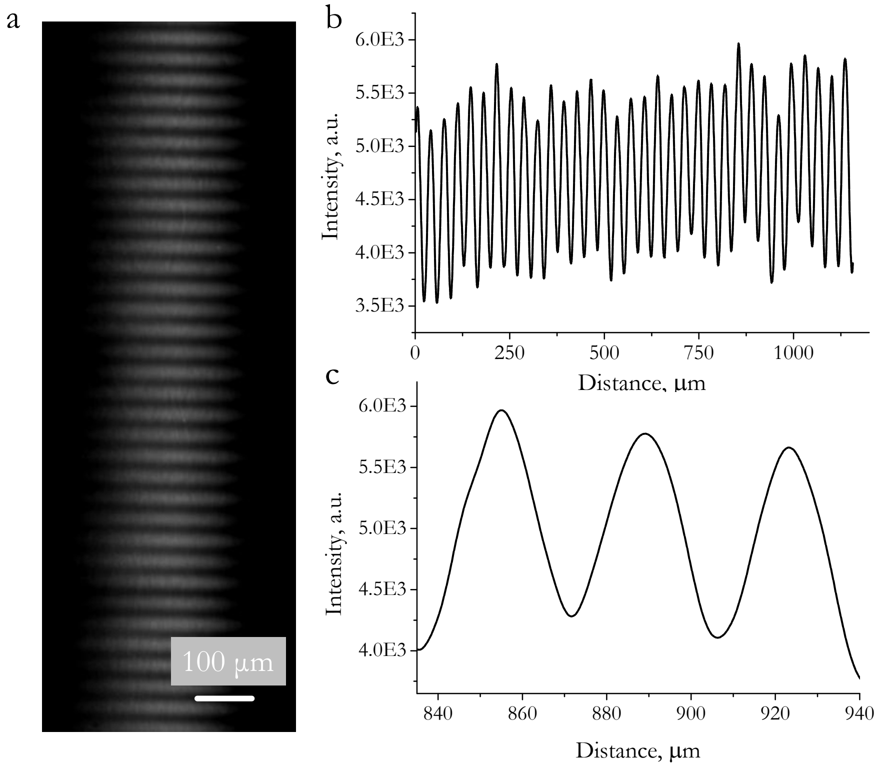

Figure 6.9. An interference pattern generated by Triacanta recorded with 65 keV – (a). The intensity variation obtained for the line though the centre of the fringe pattern – (b). An insert showing a visibility of approximately 0.17 – (c).

In order to characterize the interferometer with 65 keV the fractional Talbot image $n = 2$ which correspond to $z_2' = 53$ m was registered. To reduce secondary sources generation distance the structure with the largest number of lenses, namely, 243 was used. The lens focal distance was in order of 7 cm. The observed interference pattern together with the intensity variation obtained for the line through the centre of the fringe pattern is shown in figure 7.9. The registered fringe spacing of 36 μm is in full agreement with the theory. The measured interference fringe visibility is 0.17. It should be noted that the spatial coherence length at 65 keV is in the order of 60 μm hence only two nearest beams produced by CRLs may be suggested coherent and can interfere. The interference fringe width equals to the half of the period of the pattern; this case is identical to bilens interferometer where only two beams produced by lens can interfere. Therefore it is impossible to estimate the source size from interference fringe width as it has been made with 32 keV irradiation.

6.4 Computer simulations

A computer program based on the theory presented in section 6.2 has been created [67] to simulate the optical properties of X-ray multilens interferometers. In addition to evaluation of experimental data computer simulations allow one to estimate other experimental conditions which cannot be covered by the experiment at the moment.

For efficient use of the proposed interferometers it makes sense to address the question of the minimum period and fringe width of the interference pattern. Using the computer program the fringe pattern recorded at z_n = 12 cm fractional Talbot distance was simulated. The calculations were performed for 30 keV X-rays and the source size was chosen 10 microns. The resulting interference pattern is showed in figure 7.10. The period of the pattern is 150 nm, fringe width (FWHM) is 30 nm, and fringe visibility is close to 1. It should be noted that the depth of field of this image is in the order of 200 nm while for the focal spot of the same size it is 60 nm.

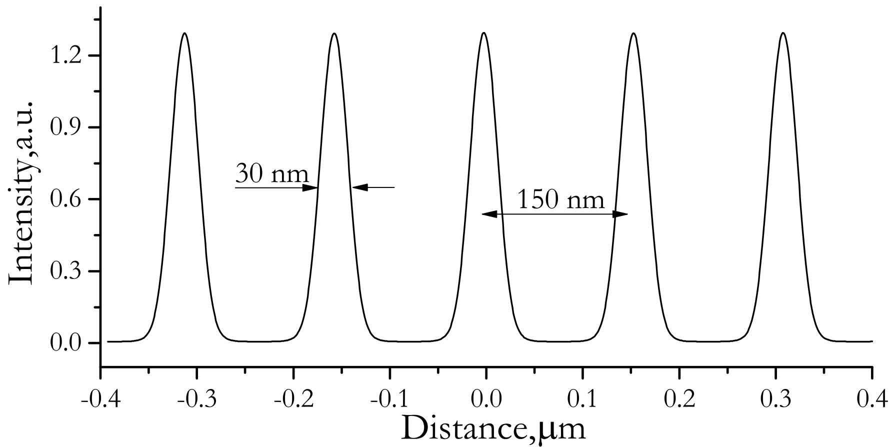

Figure 6.10. Calculated interference pattern generated by sixlens interferometer for 10 µm source size at 30 keV X-rays.

Because of the poor spatial coherence during high energy tests of the interferometer (at ID 11) it was impossible to obtain high contrast interference pattern with the high energy of irradiation. Consider the 30-lens interferometer under the illumination of 65 keV photon energy with the source size of 2 µm located at the distance of 100 m. In this case the transverse coherent length l_{coh} = 954 µm that is slightly greater than the

interferometer aperture A_1. The interference patterns were calculated at the various distances near the second Talbot image (n = 2, z_2' = 30.992 m) for the interferometer. The calculated curves showed the Talbot fringes with the period about 20 μm and with the width twice larger than $w_t \approx (0.92/M)\, d/2 \approx 0.46$ μm (see equation (6.10)). However there are two other fringes in between the Talbot fringes of a comparable intensity. Figure 6.11 shows the intensity distribution along optical axis around Talbot image.

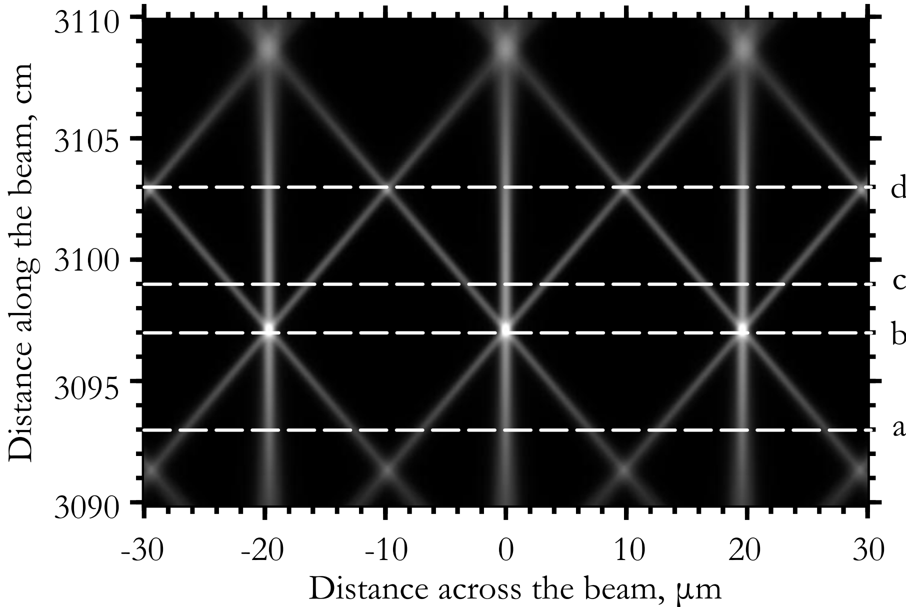

Figure 6.11. 2D relative intensity distribution as a grey contrast map with the distance across a beam horizontally and the distance along a beam vertically. The distances along the beam cover the depth of Talbot image. Dashed lines represent position of cross sections presented in figure 6.12.

The depth of field of Talbot fringes (regarding to the criteria I mentioned earlier) is equal to $w_l \approx 8.44 w_t^2/\lambda \approx 9.4$ cm (equation 6.11). The Talbot fringes are located on all observation distances at the same position across the beam (vertical lines on figure 6.11) and only their intensity (brightness in the image) is changing with the distance along the beam. On the other hand, the additional fringes change their position rather quickly. In addition to 2D intensity distribution on figure 6.12 are presented 4 cross section of it. At the distances z = 30.93 m (a) and 31.03 m (d) two fringes coincide and form one fringe in between the Talbot fringes with the intensity greater than the Talbot fringes. At the distances z = 30.97 m (b)

and 30.99 m (c) the additional fringes coincide with the Talbot fringes and make them more intense. At the all distances the clear Talbot structure can be seen.

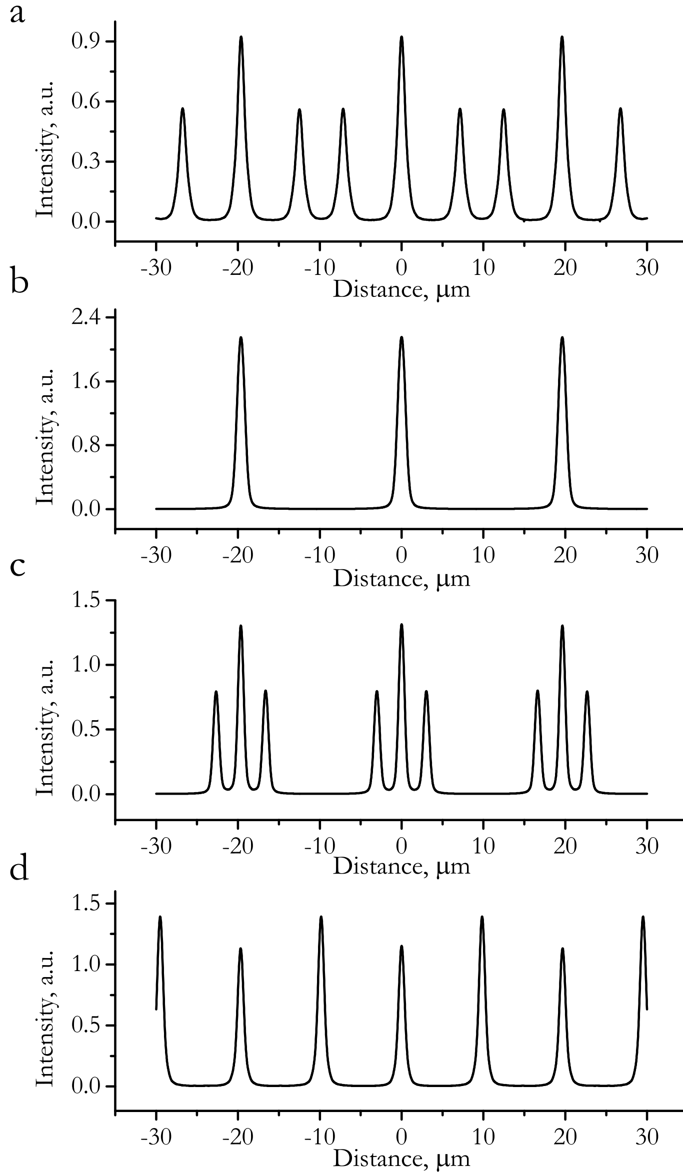

Figure 6.12. Computer simulations of interference fringes for various distances: 30.93 m – (a), 30.97 m – (b), 30.99 m – (c) and 31.03 m – (d) from the interferometer to the detector respectively. The exact Talbot distance 30.992 m is close to the (c) panel.

The reason of the appearance of additional fringes is the diffraction of X-rays at the borders of CRLs physical apertures. Indeed at the border of aperture transmission of X-ray wave is about 40%. So there are two periodic objects: a grating formed by the lens physical apertures and the foci grating. The coherent superposition of waves from these gratings in a space led to arising of “extra” fringes on the interference pattern. Therefore it is possible to eliminate additional fringes by increasing formally the absorption of the CRL material.

6.5 Discussion

Multilens interferometers were designed and manufactured for hard X-rays. Although all sets were designed for the X-ray energy range from 10 to 50 keV, in reality the energy diapason can be extended. The experimental tests covered the energy range 10 – 65 keV and near and far field observation distances.

Narrowing of the interference fringe width produced by multilens interferometers was confirmed experimentally through comparison with a bilens system during near field experiments. The enhancement of the fringe contrast was observed as well. The depth of field was studied and it is shown (theoretically by the equation 6.11) that it changed with the fraction of Talbot distance. Even for the fringe size of 30 nm, the depth of field is 4 times greater compared to a CRL focusing with the same focal spot size.

More than 90% interference fringe contrast was produced by the multilens interferometer under point source illumination. This showed that structures have very good quality and do not show a diffuse scattering in refraction geometry.

The experimental test with 65 keV irradiation confirmed that the new interferometer is fully operational with X-rays of high energies. Since the spatial coherent length for high energy was only 60 μm it was impossible to obtain high interference fringe contrast.

The computer simulations of the interference fringes for 65 keV photon energy under the condition of coherent illumination (source size 2 μm, distance to source 100 m) provided the possibility to discover a new kind of fringes due to the diffraction on the border of the CRL aperture where the transmission of radiation is rather essential.

6.6 Applications

The opportunity of direct reproducing of the object on fundamental Talbot image was used for the source size determination in section 7.3. The measured value is in full agreement with the result obtained with another technique.

In addition to the source size determination such interferometer may be used as a wavefront diagnostic device in the focusing mode such Shack – Hartmann wavefront sensor [68]. The shape of the wave field may be determined from the shift of the focal spots relative to "plane" case. Moreover the wavefront sphericity may be determined from the Talbot images position [69].

It should be noted that the proposed interferometer can be applied for electrochemical X-ray photolithography resulting in a direct non-contact pattern transfer onto an electrodeposited metal film [52]. Nanometer scale interference fringe pattern in combination with the short lifetime of radiolysis products and with a small spur radii and electron inelastic mean free paths in condensed matter will provide a possible means to rapidly improve the ultimate resolution of the proposed method to tens of nanometers (Talbot assisted lithography).

This simple way to create an X-ray standing wave in paraxial geometry opens up the opportunity to develop new X-ray interferometry techniques to study natural and advanced man-made nanoscale materials, such as self-organized bio systems, photonic and colloidal crystals, and nanoelectronics materials. As a classical interferometer it can be used for phase contrast imaging and moiré radiography. Finally it can be useful for the coherence characterization of the X-rays sources and free electron lasers.

Special place is occupied by applications related to the beam conditioning. Such interferometer can be used as a coherent versatile array illuminator or beam smoother for diffraction limited storage rings and FELs [70].

7. Micro mirrors interferometer

The apparent advantage of interferometers based on the total external reflection is that the projected length of the mirrors to the observation plane is very small, making it equivalent to the Young's interferometer with narrow slits of sub micrometer size. Especially for hard X-rays it is challenging to manufacture non transparent narrow slits. The first attempts to perform experiments with separated mirrors I described in section 4.2. Another approach, based on the differences between the critical reflection angles of two materials, was used to study the interference of reflected x-ray beams by thin gold stripes plated on the flat glass surface [71]. In the angular interval between the critical angles of substrate and coating, the ratio of the two material reflection coefficients, (R_{coat}/R_{sub}) is more than 100. However, outside this angular interval this ratio is much smaller and causes a weaker contrast of the interference fringes. To expand the angular interval of the interferometer operation, a setup with monolithic mirrors made from a Si crystal by removing a central part was proposed and used to measure the degree of spatial coherence of hard X-rays [65].

Micro-fabrication technology I described in chapter 2 allowed to manufacture deep structures with very high quality of vertical sidewalls even enough for obtaining total external reflection of X-rays. Using this advantage the interferometer based on parallel mirrors located one under another has been manufactured.

7.1 The concept of the interferometer

SEM image of bi-mirror interferometer is presented in figure 7.1. The interferometer consists of two identical vertically arranged mirror channels made in the silicon crystal. The total length of the channels *b* is 20 mm, and they are 10 μm wide. The thickness of the Si bars or slabs is 10 μm, so the mirror split distance *D* is 20 μm.

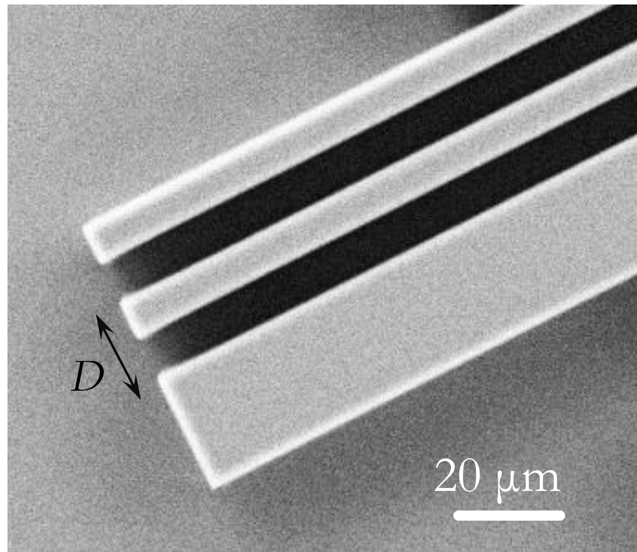

Figure 7.1. SEM image of bi-mirror interferometer manufactured in Si crystal

The novelty of this interferometer is that the reflecting surfaces are arranged vertically one above the other, while in former interferometers they are placed sequentially one after another. This design provide the reduction of the vertical gap *D* between the mirrors, which allows increase the contrast of the interference pattern in the case of poor spatial coherence, and furthermore to observe the far-field interference pattern at much shorter distances.

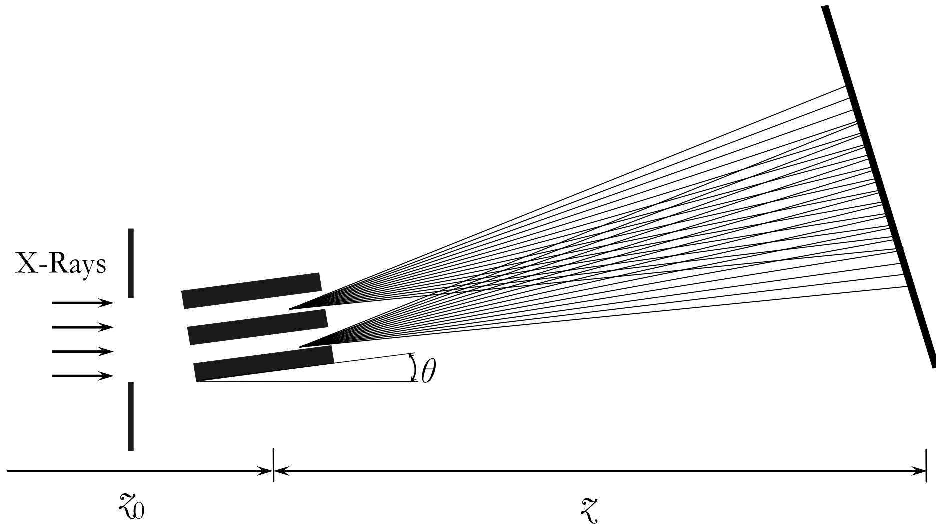

Figure 7.2. Schematic design of bi-mirror interferometer operation.

The schematic design of a bi-mirror interferometer is shown in figure 7.2. At grazing incidence angles, the vertical sidewall surface of channels resembles a mirror. The X-ray beam reflects from the sidewalls and at some distance the diffracted cones overlap, giving rise to the interference in this region. According to the Huygens–Fresnel principle, mirrors at grazing angles can be considered as secondary radiation sources. The size of each secondary source is equal to the slit width of the equivalent Young interferometer and can be modified by changing the angle θ between the incident beam and a mirror surface.

So there are two “virtual” slits with size d as a function of the grazing angle θ, namely, as a projection of the mirror length $d(\theta) = b \sin \theta$, where b is the total length of the mirror surface. Since the distance between “virtual” slits is affected weakly by the grazing incidence angle which is less than 0.1°, it is possible to exclude it from the consideration and assume the gap between slits D is constant. In comparison with the sequential arrangement of mirrors, in which D changes with the angle of incidence this is an advantage. In other words it remains unchanged the period of the interference patter during the rotation of the interferometer.

Similar to the Young double-slit scheme, the split distance D of the bi-mirror should be smaller than a spatial coherence length of the incoming beam. The intensity distribution in the far-field diffraction pattern is formed as the result of overlap between waves diffracted on two virtual slits similar to Young interferometer which I described in section 4.2:

$$I(x) = I_0 \operatorname{sinc}^2(k_d x)\left[1 + Q\cos(k_D x)\right] + I_b, \tag{7.1}$$

where

$$k_d = \frac{2\pi d}{\lambda z}, k_D = \frac{2\pi D}{\lambda z}, Q == \operatorname{sinc}\left(\pi DS / \lambda z_0\right) \tag{7.2}$$

The observed intensity pattern is characterized quantitatively by Michelson visibility parameter (equation (4.4)).

From (7.1) it follows that, for coherent radiation ($I_b = 0$) maximum and minimum adjacent intensities are:

$$I_{\max} = I_0(1+Q) \tag{7.3}$$

$$I_{\min} = I_0 \operatorname{sinc}^2\left(\pi d / D\right)(1-Q) \tag{7.4}$$

7.2 The interferometer optical properties study

The experimental test of bi-mirror interferometer has been performed at the MOTB at the ESRF ID6 beamline. A liquid nitrogen cooled Si-111 double crystal, fixed exit monochromator was used to adjust x-ray energy in the range of 12–16 keV. The source size was measured by a B-fiber interferometry technique [62], and during the bi-mirror interferometer tests was in the order of 40 μm. The interferometer was mounted on the stage with all necessary rotation and translation movements at the distance of 56 m from the source (see figure 7.2). At this distance, the spatial coherence length is about 100 μm, five times larger than bi-mirror separation so the irradiation may be considered coherent. The measurement of the interference was performed with a high resolution x-ray CCD camera ("Sensicam") equipped with a fluorescence screen and an optical objective which giving 1.3 μm spatial resolution. The measurement of interference patterns was performed at different x-ray incidence angles θ, achieved by rotating the interferometer. The typical exposure time varied between 10 s and 1 min; depending on the incidence angle and observation distance, the storage ring mode was 7/8 + 1 with a current approximately 200 mA. To characterize the interferometer in the near-field, 12 keV were chosen and a CCD was placed downstream from the interferometer at the distance z = 1.5 m. The observed interference pattern and intensity variation obtained for the line through the center of the fringe pattern measured at a grazing incidence angle of $\theta = 0.004°$ are shown in figure 8.3.

The cross section of interference pattern measured at a grazing incidence angle of $\theta = 0.007°$ is presented in figure 7.3 (c). The quantitative evaluation of interference patterns was performed by the visibility parameter V, calculated in the center of the pattern in a region of maximum overlap of diffracted beams. These incidence angles correspond to the mirror projection or "virtual" slit sizes of d = 1.4 μm and d = 2.5 μm, respectively.

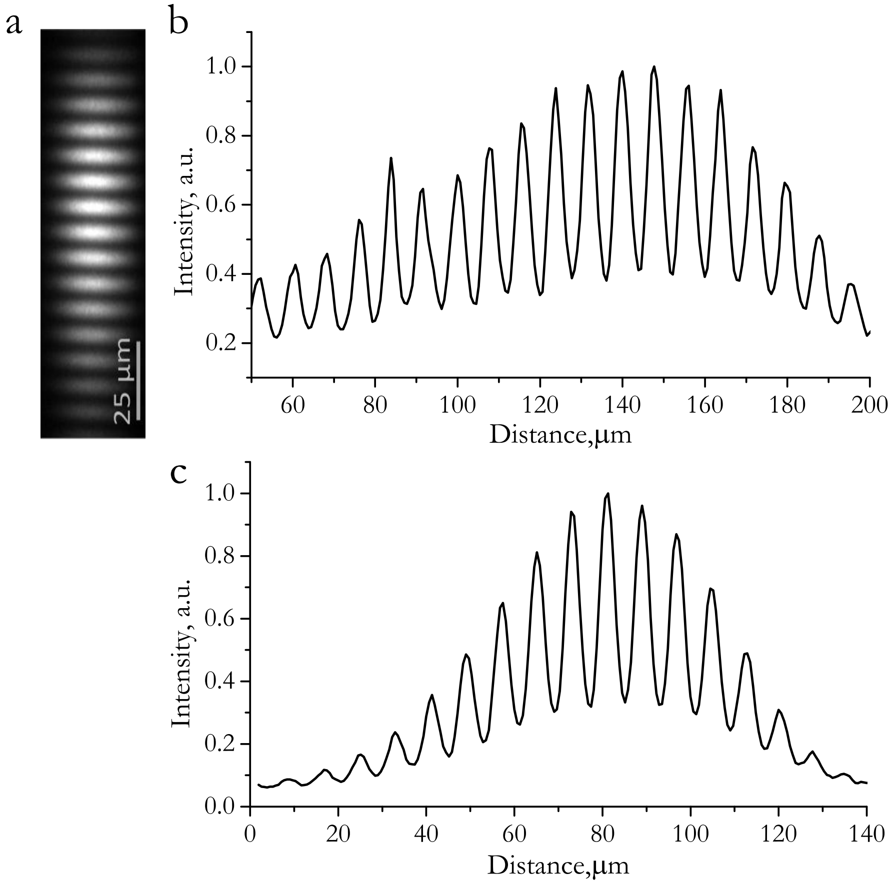

Figure 7.3. Interference pattern – (a), the intensity variation obtained for the line through the fringe centre recorded at an incidence angle of 0.004°– (b) and the intensity variations for the interference pattern registered at an incidence angle of 0.007°– (c).

The interference fringe visibility corresponding to the lower angle θ = 0.004° is 0.58, whereas for the angle θ = 0.007° the visibility is 0.545. Increasing the incident angle of the primary beam leads to a reduction of the mirror diffraction cones resulting in the narrowing of the overlapping area which in turn reduces the contrast. It is evident that, to obtain reliable experimental data, which can be easily interpreted, it is necessary to measure the interference pattern in the far-field. Taking into account the beamline characteristics such as energy range, available distances, and efficiency of the CCD camera, the far-field tests of the bi-mirror interferometer were performed at 16 keV photon energy (0.77 Å wavelength) and at mirror-to-detector distance z = 15 m. It can be easily estimated that for this photon energy and 20 µm bi-mirror separation the far-field observation distance

(the region of Fraunhofer diffraction) must be much larger than $z = D^2/\lambda \approx$ 5 m.

The far-field intensity variations obtained for the line through the center of the fringe pattern recorded at angles of incidence θ = 0.009° and θ = 0.021° are depicted in figure 7.4 (a) and (b). Contrary to near field measurements, the maximum measured visibility of 0.86 corresponds to the higher incident angle, a clear demonstration that far-field conditions are fulfilled. Figure 8.4 (c) presents the dependence of fringe visibility on the incidence angle. Depending on the incident angle, the contrast of the fringes varied within 0.1, steadily increasing with incident angle. However, I would like to stress that the calculated fringe visibility for a 40 µm source is about 0.95, and the changing of the incidence angle does not affect significantly the contrast (for example, a doubling of the grazing incidence angle from 0.01° to 0.02° increases the fringe visibility from 0.93 to 0.95). The formally estimated source size from the bi-mirror fringe visibility at a grazing incidence angle of θ = 0.009° is S = 78 µm, while for angle θ = 0.021° is S = 55 µm that is essentially closer to the result of the B-fiber S = 40 µm. The reduction of the fringe contrast and its pronounced angular dependence can be caused by diffuse scattering resulting from the roughness of the etched surface. To estimate this effect, evaluation of the surface roughness from the visibility of interference fringes has to be performed.

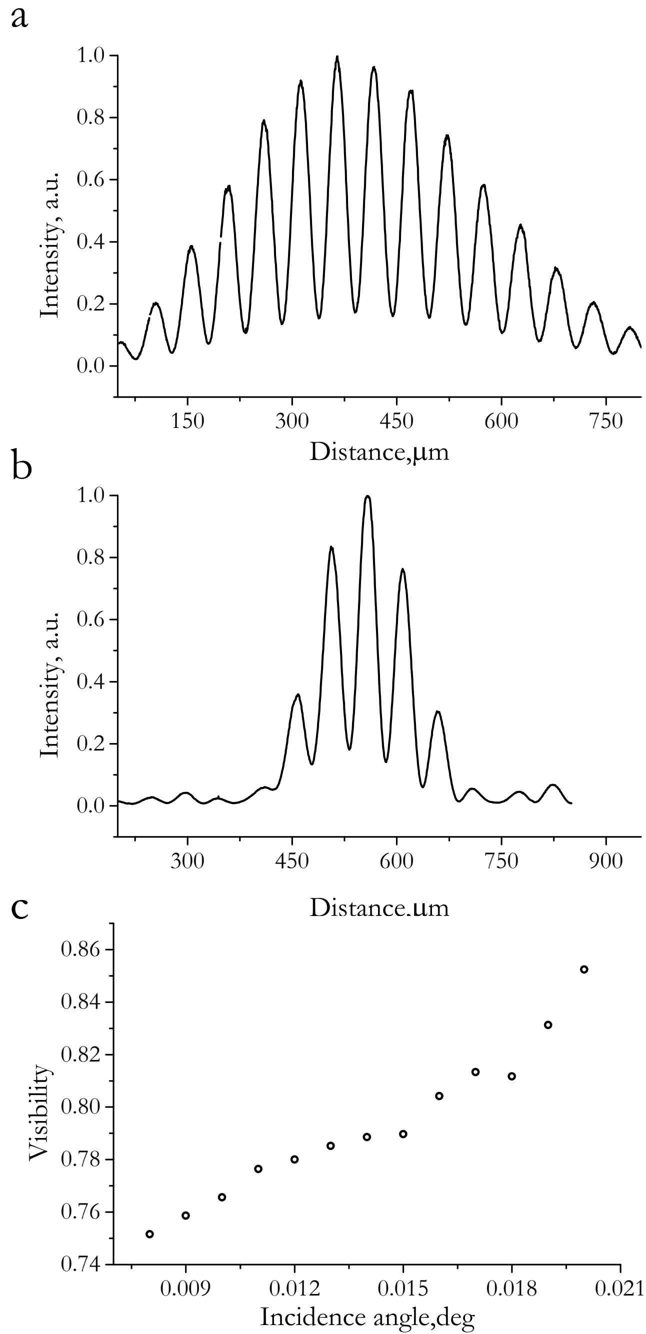

Figure 7.4. Interference pattern vertical cross section for an incidence angle of 0.009° – (a), cross section of the interference pattern for an incidence angle of 0.021°– (b), and angular dependence of the fringe visibility – (c).

7.3 Applications

As has been shown earlier the interference fringe visibility is affected not only by angular source size but also the surface roughness. To estimate this effect an evaluation of the surface roughness from the fringe visibility has been made.

The experiment was carried out under grazing incidence and reflection conditions, where the angles of incidence are much less than the critical angle of total reflection θ_c, which for Si is between 0.15° and 0.11° in the photon energy range of 10–16 keV. In this case, the specularly reflected component of the scattering should be analyzed as the Fresnel reflectivity.

Roughness reduces the reflected amplitude; therefore, it is necessary to consider its influence in the Fresnel equations introducing the damping factor. To take into account the contribution of the roughness in the Fresnel reflectivity, the well known Gaussian damping, given by Rayleigh, is the most widely used, although it does not fully describe the measured intensity of the reflected of X-rays [72, 73]. If a surface roughness is small and if a Gaussian distribution of roughness heights is assumed, the specular intensity can be written as:

$$I = I_0 \exp\left(-4k^2\theta^2\sigma^2\right) \tag{7.5}$$

where θ is the grazing angle of the reflection. To obtain a more appropriate description of the reflectivity in the vicinity of the critical angle, an improved expression for the damping factor, where it is assumed the loss of the coherence of the x-ray wave on the rough surface, was proposed in [73]. However, this approach is not suitable for grazing angles of much less than the critical angle.

Using (7.5) and the Michelson visibility (4.4), the irradiances I^T_{max} and I^T_{min}, corresponding to the maximum and adjacent minimum of the interference pattern will be:

$$I^T_{max} = I_0 \exp\left(-4k^2\theta^2\sigma^2\right)\left(1+Q\right) \tag{7.6}$$

$$I^T_{min} = I_0 \exp\left(-4k^2\theta^2\sigma^2\right)\times \mathrm{sinc}^2\left(\pi\frac{d}{D}\right)\times\left(1-Q\right) \tag{7.7}$$

I assumed that all the background intensity consists of the diffuse part of the reflected beam (the absorption is neglected):

$$I_b = I_0\left[1-\exp\left(-4k^2\theta^2\sigma^2\right)\right] \tag{7.8}$$

and that the visibility V_{exp}, calculated from the experimental data of intensity cross sections should be expressed theoretically by taking into account background intensity:

$$V_{exp} = \frac{I_{max}^T - I_{min}^T}{I_{max}^T + I_{min}^T + 2I_b} \tag{7.9}$$

If the surface roughness and grazing angle of the reflection are very small, then it is possible to replace the exponent by the sum, $\exp(4k^2\theta^2\sigma^2) \approx 1+4k^2\theta^2\sigma^2$, and, from expressions (7.6) – (7.9), the value of the dumping factor and hence the rms surface roughness are obtained as:

$$4k^2\theta^2\sigma^2 = \frac{1}{2}\left\{(1+Q)+(1-Q)\operatorname{sinc}^2\left(\pi\frac{d}{D}\right)\right\}\left[\frac{V_T}{V_{exp}}-1\right] \tag{7.10}$$

where V_T is the theoretical visibility calculated by (4.4), (7.3) and (7.4).

For example, a measured visibility of 0.87 at a grazing incidence angle of 0.021° gives an rms surface roughness σ = 55 Å, whereas for a measured visibility of 0.77 at a grazing incidence angle of 0.009° corresponds to an rms surface roughness σ = 185 Å. I notice that, from estimations mentioned above, the influence of the surface roughness on the visibility at very small incident angles is more pronounced and results in a low value of fringe contrast. Such a large difference in the roughness results from the limitation of the proposed roughness evaluation model. It should be noted that the surface after the reactive-ion etching process used to produce Si trenches has a very complex topography [23] resulting in a strongly varying power spectral density (PSD). I do not exclude that the spatial frequencies probed are diverse enough so that very different integrals of PSD could result.

The etched surface of the trenches has been studied by SEM; at least three different spatial frequencies of the surface roughness were observed: 5 nm 15 nm and 200 nm. The SEM images are presented in figure 7.5.

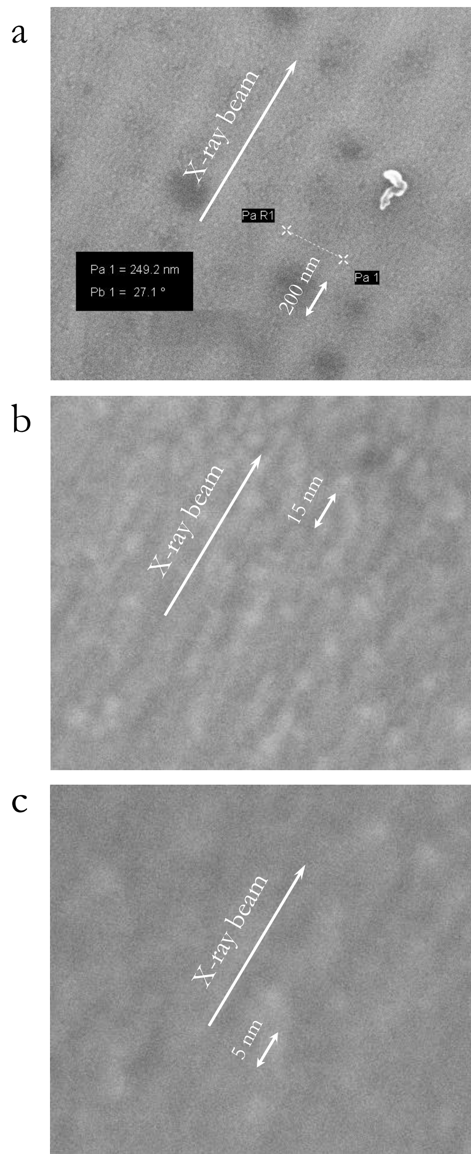

Figure 7.5. SEM images of the etched surface of trenches. Three different roughness periods were detected 200 nm – (a), 15 nm – (b), and 5 nm – (c).

Despite the fact that the surface roughness evaluation I expressed above is very approximate one may draw the conclusion that this interferometer is applicable for the study of the quality of the etched surface. An express study of the quality by modification of the fringe visibility of the interference pattern may be performed just by registering the interference

patterns. In addition, without determination of roughnesses, the quality of the etched surfaces of structures which were etched differently during the estimation of the parameter of etching process may be compared quantitatively.

Apart from roughness study this interferometer is applicable for classical interferometric experiments, such coherence study or phase contrast imaging. This new design allowed the creation of reflecting surfaces at any split distance. The close arrangement of mirrors provided the possibility to observe high contrast interference pattern for sources with poor spatial coherence such as X-ray laboratory sources.

7.4 Discussion

The bi-mirror interferometer for hard X-rays was designed and manufactured in a Si crystal using microfabrication planar technology. This new design allowed the creation of reflecting surfaces at any split distance.

The close arrangement of mirrors makes it possible to observe high contrast interference pattern for sources with poor spatial coherence such as X-ray laboratory sources. The bi-mirror was experimentally tested in the near and far-field conditions. The quality of the etched sidewall surfaces is sufficient to register interference patterns with a fringe visibility of 0.86. The decrease of fringe visibility, especially noticeable at small grazing angles, results from the diffuse scattering resulting from the surface roughness of mirrors. A model, based on rather simple and approximate assumptions, was considered for the evaluation of the influence of the channel surface roughness on the visibility of interference fringes. A roughness of the etched surface smaller than 185 Å rms was estimated based on the collected data, and it is in a good agreement with previous results [8]. This bi-mirror interferometer is implemented on a multifunctional x-ray silicon chip which includes other optical elements such as compound parabolic refractive lenses [14], bi-lens [3], and multi-lens interferometers based on refractive lenses [15]. Microfabrication technology, used in the manufacturing of the universal silicon chip, ensures that the bi-mirror interferometer reflective surfaces, made simultaneously with the compound refractive parabolic lenses, are identical in surface roughness. Therefore, the assessment of roughness obtained from bi-mirror interferometry data will be valuable for the evaluation of the focusing properties of the compound refractive lenses and, obviously, for improvement of the technological processes.

8. Conclusions

The availability of brilliant and highly coherent beams due to 3rd generation synchrotrons and free electron lasers together with the development of Si structuring technologies has opened up a new chapter of X-ray science and technology. Many experimental techniques, such as phase contrast imaging [20] microscopy [74] or interferometry [64] have been transferred to the field of X-ray science. In this dissertation, the development, characterization and application of three new interferometric schemes in the hard X-ray region are presented.

Understanding the spatial coherence properties of irradiation is required for the design and manufacturing of optical elements, for planning and analyzing experiments. Differently from the region of visible light, X-ray region cannot boast of well studied coherent properties of the beam. Consequently the first scheme is aimed to the characterization of the source size on small emittance storage ring; it is tunable double slit interferometer. The variable distance between slits overcome the problem of technique sensitivity to the source size on small emittance storage rings. At the same time the use of refractive lens eliminated the issue of large far field observation distance for large slits separations. The new demonstrated approach for the planning and analyzing of the experiment provided the possibility to measure the size of the source on ultimate storage rings with submicron precision in wide energy range starting from soft X-rays and up to hundred of keV.

The next scheme is multilens interferometer. Two interferometers, consisting of 30 and 6 lens arrays were manufactured and tested. Experimental tests have been performed in the wide energy diapason – from 12 to 64 keV. Experimental results showed full agreement with theory which confirms that structures are manufactured with very high quality. The effective source size was determined with high precision by analyzing the fundamental Talbot image formed by multilens interferometer with high energy of irradiation. The specific of forming of interference pattern in the far field allows one to use this interferometer as a tool to diagnose the sphericity of the incident wavefront. In addition such lens array is possible

to use as an advanced Shack-Hartmann [68] wavefront sensor in focusing mode.

The possibility of forming the standing wave in paraxial geometry with variable period and maxima width opened up a new prospective in using this interferometer in investigation of nano objects without deposition on the flat surface (standing wave technique [75]). The large depth of field of interference fringe (in comparison with the focal spot of the same size) made it possible to use this interferometer for the purpose of transmission scanning microscopy and moiré radiography of nano objects.

The applications related to the beam conditioning can be attributed to a special group. This interferometer may be used as a beam expander or versatile illuminator [70] to provide coherent illumination of large scale object on FELs and ultimate storage rings. Finally the lens array based interferometers may be used for phase contrast imaging.

The last interferometric scheme is single crystal double mirror. It was discovered, during the study of the optical properties of multilens interferometers that quality of the etched surface of structures allows one to obtain TER of X-rays. The bi – mirror interferometer consisting of two parallel channels was manufactured on the same Si chip as sixlens interferometer. The sensitivity of the interference contrast to the angle of incidence was found. This indicates the presence of impact of scattering of X-rays on surface roughness to the interference pattern formation. The evaluation of surface roughness was performed. This allows saying that this interferometer may be used as express roughness diagnostic tool. The possibility to locate reflective surfaces very close to each other made it possible to observe high contrast interference pattern for sources with poor spatial coherence such as X-ray laboratory sources.

List of symbols

n	1. Ccomplex refractive index
	2. Arbitrary integer
δ	Real part (decrement) of n, the index of the refraction
β	1. Imaginary part of n, the index of the refraction
	2. Coefficient in Lorentz factor
	3. Function related to transverse size of e-beam
$f^0(\omega)$	Complex atomic scattering factor
r_e	Classical electron radius
e	Electron elemental charge
λ	Wavelength
n_a	Number of atoms of type a
μ	Linear absorption coefficient
τ	Photoabsorption coefficient
μ_R	Elastic scattering absorption coefficient
μ_C	Inelastic scattering absorption coefficient
E	Photon energy
d	Thickness of the material
Φ	Phase of the wave
k	Wavenumber
n_V	The complex refractive index for vacuum (equals to 1)
θ_c	Total external reflection critical angle
m_0	Electron rest mass
c	Speed of light in vacuum
h	Planck constant
ε_v, ε_h	Vertical and horizontal emittance
σ_v, σ_v'	Vertical size of electron beam and divergence
K	Dimensionless parameter of the ID
B_0	Peak magnetic field
λ_u	ID period
α_{max}	Maximum deflection angle of electrons in the storage ring
α	1. Angle between mirror and primary beam
	2. Parameter in an equation

	3. Angular source size
γ	1. Lorentz factor
	2. Complex degree of coherence
l_1	Longitudinal coherence length
v	Speed of electrons in the storage ring
F	The compound refractive lens focal length
R	1. Radius of curvature of single refractive lens
	2. Reflection coefficient
T	Lens transmission
σ	Surface rms roughness
A	Term in an equation
A_{eff}	Effective aperture of CRL
A_{phys}	Physical aperture of CRL
A_{i}	Multilens interferometer aperture
r	1. The lateral resolution of CRL
	2. Distance in real space
	3. Ray path
U	Field
x, y, z	Coordinate system with z axis along the optical axis
ξ,η	Coordinates in the diffraction geometry
V	Michelson visibility parameter
z_{T}	Talbot distance
p, q, m, j	Arbitrary integers
Γ	Mutual coherence function
t,τ	Time and time interval
I	Intensity
l_1	Longitudinal coherence length
V	Michelson fringe visibility
l_{coh}	Spatial coherence length
S	Source size
Λ	Fringe spacing
S'	Size of the image of the source
R_{d}	Projection of fiber radius to the detector plane
D	Distance between slits
D_{V}	Dispersion
d	1. Thickness of sample
	2. Size of the slit
	3. Period of multilens interferometer
w_l	Transverse vertical fringe size of multilens interferometer
w_t	Longitudinal fringe size of multilens interferometer
Δ	Difference

b	Total length of channel of bi-mirror interferometer
M	Number of lens arrays in multilens interferometer
N	Number of individual lenses in CRL
I	Intensity

List of abbreviations

FZP	Fresnel zone plate
RL	Refractive lens
ESRF	European Synchrotron Radiation Facility
MEMS	Micro electro mechanical systems
FEL	Free electron laser
NFL	Nanofocusing lenses
ID	Insertion device
BM	Bending magnet
MOTB	Micro optics test bench
CCD	Charge coupled device
CRL	Compound refractive lens
rms	Root mean square
N.A.	Numerical aperture
DoF	Depth of focus
e-beam	Electron beam
SEM	Scanning electron microscope
FReLoN	Fast readout low noise camera
RIE	Reactive ion etching
FWHM	Full width at half maximum
TER	Total external reflection
PSD	Power spectral density

Bibliography

1. J. B. Pawley, and B. R. Masters, "Handbook of Biological Confocal Microscopy, Second Edition," in *Optical Engineering* (1996), pp. 2765-2766.
2. D. D. Nolte, *Interferometry* (Springer, New York, 2012).
3. T. Young, *A course of lectures on natural philosophy and the mechanical arts. By Thomas Young* (Printed for J. Johnson, London, UK, 1807).
4. L. Rayleigh, "XXV. On copying diffraction-gratings, and on some phenomena connected therewith," Philosophical Magazine Series 5 **11**, 196-205 (1881).
5. F. Zernike, "The concept of degree of coherence and its application to optical problems," Physica **5**, 785-795 (1938).
6. A. Sommerfeld, *Lectures on Theoretical Physics* (Academic Press, New York, 1954).
7. W. D. Montgomery, "Self-Imaging Objects of Infinite Aperture," Journal of the Optical Society of America **57**, 772-775 (1967).
8. J. W. Goodman, *Introduction to Fourier Optics* (McGraw-Hill Book Company, New York, US, 1968).
9. D. Attwood, K. Halbach, and K.-J. Kim, "Tunable Coherent X-rays," Science **228**, 1265-1272 (1985).
10. A. Snigirev, I. Snigireva, V. Kohn, S. Kuznetsov, and I. Schelokov, "On the possibilities of x-ray phase contrast microimaging by coherent high-energy synchrotron radiation," Review of Scientific Instruments **66**, 5486-5492 (1995).
11. R. Coïsson, "Spatial coherence of synchrotron radiation," Applied Optics **34**, 904-908 (1995).

12. A. Momose, "Demonstration of phase-contrast X-ray computed tomography using an X-ray interferometer," Nuclear Instruments and Methods in Physics Research Section A: Accelerators, Spectrometers, Detectors and Associated Equipment **352**, 622-628 (1995).
13. C. Raven, A. Snigirev, I. Snigireva, P. Spanne, A. Souvorov, and V. Kohn, "Phase-contrast microtomography with coherent high-energy synchrotron x rays," Applied Physics Letters **69**, 1826-1828 (1996).
14. A. R. Lang, and A. P. W. Makepeace, "Production of synchrotron X-ray biprism interference patterns with control of fringe spacing," Journal of Synchrotron Radiation **6**, 59-61 (1999).
15. M. Grigoriev, L. Shabelnikov, V. Yunkin, A. A. Snigirev, I. Snigireva, M. Di Michiel, S. Kuznetsov, M. Hoffmann, and E. I. Voges, "Planar parabolic lenses for focusing high-energy x-rays," in *Proc. SPIE Int. Soc. Opt. Eng.*(2001), pp. 185-192.
16. D. Paterson, B. E. Allman, P. J. McMahon, J. Lin, N. Moldovan, K. A. Nugent, I. McNulty, C. T. Chantler, C. C. Retsch, T. H. K. Irving, and D. C. Mancini, "Spatial coherence measurement of X-ray undulator radiation," Optics Communications **195**, 79-84 (2001).
17. D. G. Lee, J. J. Park, J. H. Sung, and C. H. Nam, "Wave-front phase measurements of high-order harmonic beams by use of point-diffraction interferometry," Optics Letters **28**, 480-482 (2003).
18. A. Snigirev, V. Kohn, I. Snigireva, and B. Lengeler, "A compound refractive lens for focusing high-energy X-rays," Nature **384**, 49-51 (1996).
19. G. Schmahl, D. Rudolph, P. Guttmann, and O. Christ, "Zone Plates for X-Ray Microscopy," in *X-Ray Microscopy*, G. Schmahl, and D. Rudolph, eds. (Springer Berlin Heidelberg, 1984), pp. 63-74.
20. T. Takeda, A. Momose, Y. Itai, W. Jin, and K. Hirano, "Phase-contrast imaging with synchrotron x-rays for detecting cancer lesions," Academic Radiology **2**, 799-803 (1995).
21. W. Leitenberger, S. M. Kuznetsov, and A. Snigirev, "Interferometric measurements with hard X-rays using a double slit," Optics Communications **191**, 91-96 (2001).
22. A. Momose, S. Kawamoto, I. Koyama, Y. Hamaishi, K. Takai, and Y. Suzuki, "Demonstration of X-Ray Talbot Interferometry," Japanese Journal of Applied Physics **42**, L866 (2003).

23. A. Snigirev, I. Snigireva, M. Grigoriev, V. Yunkin, M. Di Michiel, S. Kuznetsov, and G. Vaughan, "Silicon planar lenses for high-energy x-ray nanofocusing," in *Proc. SPIE Int. Soc. Opt. Eng.*(2007), p. 670506.
24. A. Snigirev, I. Snigireva, V. Kohn, V. Yunkin, S. Kuznetsov, M. B. Grigoriev, T. Roth, G. Vaughan, and C. Detlefs, "X-Ray Nanointerferometer Based on Si Refractive Bilenses," Physical Review Letters **103**, 064801 (2009).
25. W. C. Röntgen, "Über eine neue Art von Strahlen," Physikalisch-medizinische Gesellschaft (1895).
26. J. Als-Nielsen, and D. McMorrow, *Elements of Modern X-ray Physics* (John Wiley & Sons, Inc., New York, US, 2001).
27. R. W. James, and W. L. Bragg, *The optical principles of the diffraction of x-rays* (G. Bell & Sons, London, UK, 1962).
28. E. Hecht, *Optics (4th Edition)* (Addison Wesley, San Francisco, US, 2001).
29. P. Beckmann, and A. Spizzichino, *The Scattering of Electromagnetic Waves from Rough Surfaces* (Artech House, Norwood, US, 1987).
30. M. Lyubomirskiy, I. Snigireva, S. Kuznetsov, V. Yunkin, and A. Snigirev, "Hard x-ray single crystal bi-mirror," Optics Letters **40**, 2205-2208 (2015).
31. A. Franchi, L. Farvacque, J. Chavanne, F. Ewald, B. Nash, K. Scheidt, and R. Tomás, "Vertical emittance reduction and preservation in electron storage rings via resonance driving terms correction," Physical Review Special Topics - Accelerators and Beams **14**, 034002 (2011).
32. K. Holldack, J. Feikes, and W. B. Peatman, "Source size and emittance monitoring on BESSY II," Nuclear Instruments and Methods in Physics Research Section A: Accelerators, Spectrometers, Detectors and Associated Equipment **467–468, Part 1**, 235-238 (2001).
33. B. Lengeler, C. G. Schroer, M. Richwin, J. Tümmler, M. Drakopoulos, A. Snigirev, and I. Snigireva, "A microscope for hard x rays based on parabolic compound refractive lenses," Applied Physics Letters (1999).
34. B. Lengeler, C. Schroer, J. Tummler, B. Benner, M. Richwin, A. Snigirev, I. Snigireva, and M. Drakopoulos, "Imaging by parabolic refractive lenses in the hard X-ray range," Journal of Synchrotron Radiation **6**, 1153-1167 (1999).

35. C. G. Schroer, O. Kurapova, J. Patommel, P. Boye, J. Feldkamp, B. Lengeler, M. Burghammer, C. Riekel, L. Vincze, A. van der Hart, and M. Küchler, "Hard x-ray nanoprobe based on refractive x-ray lenses," Applied Physics Letters **87**, - (2005).
36. J. Y. Zhao, E. E. Alp, T. S. Toellner, W. Sturhahn, H. Sinn, and D. Shu, "A water-cooled compound refractive lens as a white beam collimator," Review of Scientific Instruments **73**, 1611-1613 (2002).
37. G. B. M. Vaughan, J. P. Wright, A. Bytchkov, M. Rossat, H. Gleyzolle, I. Snigireva, and A. Snigirev, "X-ray transfocators: focusing devices based on compound refractive lenses," Journal of Synchrotron Radiation **18**, 125-133 (2011).
38. V. Kohn, I. Snigireva, and A. Snigirev, "Diffraction theory of imaging with X-ray compound refractive lens," Optics Communications **216**, 247-260 (2003).
39. M. Drakopoulos, A. Snigirev, I. Snigireva, and J. Schilling, "X-ray high-resolution diffraction using refractive lenses," Applied Physics Letters **86**, 014102 (2005).
40. A. V. Petukhov, J. H. J. Thijssen, D. C. 't Hart, A. Imhof, A. van Blaaderen, I. P. Dolbnya, A. Snigirev, A. Moussaid, and I. Snigireva, "Microradian X-ray diffraction in colloidal photonic crystals," Journal of Applied Crystallography **39**, 137-144 (2006).
41. A. Bosak, I. Snigireva, K. S. Napolskii, and A. Snigirev, "High-Resolution Transmission X-ray Microscopy: A New Tool for Mesoscopic Materials," Advanced Materials **22**, 3256-3259 (2010).
42. V. G. Kohn, "An exact theory of imaging with a parabolic continuously refractive X-ray lens," Journal of Experimental and Theoretical Physics **97**, 204-215 (2003).
43. B. Lengeler, C. G. Schroer, B. Benner, A. Gerhardus, T. F. Gunzler, M. Kuhlmann, J. Meyer, and C. Zimprich, "Parabolic refractive X-ray lenses," Journal of Synchrotron Radiation **9**, 119-124 (2002).
44. C. G. Schroer, B. Lengeler, B. Benner, T. F. Guenzler, M. Kuhlmann, A. S. Simionovici, S. Bohic, M. Drakopoulos, A. A. Snigirev, I. Snigireva, and W. H. Schroeder, "Microbeam production using compound refractive lenses: beam characterization and applications," in *Proc. SPIE Int. Soc. Opt. Eng.*(2001), pp. 52-63.

45. J. M. Cowley, *Diffraction Physics (Third Edition)* (North-Holland, Amsterdam, 1995).
46. H. F. Talbot, "LXXVI. Facts relating to optical science. No. IV," Philosophical Magazine Series 3 **9**, 401-407 (1836).
47. J. M. Cowley, and A. F. Moodie, "Fourier Images IV: The Phase Grating," Proceedings of the Physical Society **76**, 378-384 (1960).
48. J. T. Winthrop, and C. R. Worthington, "Theory of Fresnel Images. I. Plane Periodic Objects in Monochromatic Light," Journal of the Optical Society of America **55**, 373-380 (1965).
49. K. Patorski, "I The Self-Imaging Phenomenon and its Applications," in *Progress in Optics*, E. Wolf, ed. (Elsevier, 1989), pp. 1-108.
50. P. Cloetens, J. P. Guigay, C. De Martino, J. Baruchel, and M. Schlenker, "Fractional Talbot imaging of phase gratings with hard x rays," Optics Letters **22**, 1059-1061 (1997).
51. T. Weitkamp, A. Diaz, C. David, F. Pfeiffer, M. Stampanoni, P. Cloetens, and E. Ziegler, "X-ray phase imaging with a grating interferometer," Optics Express **13**, 6296-6304 (2005).
52. A. A. Eliseev, N. A. Sapoletova, I. Snigireva, A. Snigirev, and K. S. Napolskii, "Electrochemical X-ray Photolithography," Angewandte Chemie International Edition **51**, 11602-11605 (2012).
53. J. W. Goodman, *Statistical optics* (Wiley-Interscience, New York, US, 1985).
54. M. Born, and E. Wolf, *Principles of Optics: Electromagnetic Theory of Propagation, Interference and Diffraction of Light* (Cambridge University Press, Cambridge, UK, 1999).
55. B. J. Thompson, and E. Wolf, "Two-beam interference with partially coherent light," Journal of the Optical Society of America **47**, 895 (1957).
56. K. Fezzaa, F. Comin, S. Marchesini, R. Coïsson, and M. Belakhovsky, "X-Ray Interferometry at ESRF Using Two Coherent Beams from Fresnel Mirrors," Journal of X-Ray Science and Technology **7**, 12-23 (1997).
57. A. Momose, "Phase-sensitive imaging and phase tomography using X-ray interferometers," Optics Express **11**, 2303-2314 (2003).

58. V. Kohn, I. Snigireva, and A. Snigirev, "Direct Measurement of Transverse Coherence Length of Hard X Rays from Interference Fringes," Physical Review Letters **85**, 2745-2748 (2000).

59. U. Bonse, and M. Hart, "AN X-RAY INTERFEROMETER," Applied Physics Letters **6**, 155-156 (1965).

60. M. Françon, *Optical Interferometry* (Academic Press, New York, US, 1966).

61. M. Tegze, and G. Faigel, "X-ray holography with atomic resolution," Nature **380**, 49-51 (1996).

62. V. Kohn, I. Snigireva, and A. Snigirev, "Interferometric characterization of spatial coherence of high energy synchrotron X-rays," Optics Communications **198**, 293-309 (2001).

63. T. Weitkamp, O. Chubar, M. Drakopoulos, A. Souvorov, I. Snigireva, A. Snigirev, F. Günzler, C. Schroer, and B. Lengeler, "Refractive lenses as a beam diagnostics tool for high-energy synchrotron radiation," Nuclear Instruments and Methods in Physics Research Section A: Accelerators, Spectrometers, Detectors and Associated Equipment **467–468, Part 1**, 248-251 (2001).

64. W. Leitenberger, H. Wendrock, L. Bischoff, and T. Weitkamp, "Pinhole interferometry with coherent hard X-rays," Journal of synchrotron radiation **11**, 190-197 (2004).

65. W. Leitenberger, and U. Pietsch, "A monolithic Fresnel bimirror for hard X-rays and its application for coherence measurements," Journal of Synchrotron Radiation **14**, 196-203 (2007).

66. L. Kipp, M. Skibowski, R. L. Johnson, R. Berndt, R. Adelung, S. Harm, and R. Seemann, "Sharper images by focusing soft X-rays with photon sieves," Nature **414**, 184-188 (2001).

67. A. Snigirev, I. Snigireva, M. Lyubomirskiy, V. Kohn, V. Yunkin, and S. Kuznetsov, "X-ray multilens interferometer based on Si refractive lenses," Optics Express **22**, 25842-25852 (2014).

68. S. C. Mayo, and B. Sexton, "Refractive microlens array for wave-front analysis in the medium to hard x-ray range," Optics Letters **29**, 866-868 (2004).

69. D. Malacara-Doblado, "Measuring the curvature of spherical wavefronts with Talbot interferometry," Optical Engineering **36**, 2016-2024 (1997).

70. E. Bonet, P. Andrés, J. C. Barreiro, and A. Pons, "Self-imaging properties of a periodic microlens array: versatile array illuminator realization," Optics Communications **106**, 39-44 (1994).
71. S. Aoki, N. Watanabe, T. Ohigashi, H. Yokosuka, Y. Suzuki, A. Takeuchi, and H. Takano, "Production of Reflection Point Sources for Hard X-Ray Gabor Holography," Japanese Journal of Applied Physics **44**, 417 (2005).
72. S. K. Sinha, E. B. Sirota, S. Garoff, and H. B. Stanley, "X-ray and neutron scattering from rough surfaces," Physical Review B **38**, 2297-2311 (1988).
73. F. Stanglmeier, B. Lengeler, W. Weber, H. Gobel, and M. Schuster, "Determination of the dispersive correction f'(E) to the atomic form factor from X-ray reflection," Acta Crystallographica Section A **48**, 626-639 (1992).
74. B. Lengeler, C. G. Schroer, M. Richwin, J. Tümmler, M. Drakopoulos, A. Snigirev, and I. Snigireva, "A microscope for hard x rays based on parabolic compound refractive lenses," Applied Physics Letters **74**, 3924-3926 (1999).
75. J. Zegenhagen, "Surface structure determination with X-ray standing waves," Surface Science Reports **18**, 202-271 (1993).